

YTTRIA RICH TBCS AS CANDIDATES FOR CMAS RESISTANT TOP
COATS

JUAN JOSE GOMEZ CHAVEZ
Department of Mechanical Engineering

APPROVED:

Ramana Chintalapalle, Ph.D., Chair

Ravisankar Naraparaju, Ph.D.

Pavana Prabhakar, Ph. D.

Stephen W. Stafford, Ph.D.

Charles Ambler, Ph.D.
Dean of the Graduate School

Copyright ©

by

Juan Jose Gomez

2016

Dedication

I dedicate this work to my parents whose unconditional support and encouragement have always helped me to keep going and grow as an individual and professional.

YTTRIA RICH TBCS AS CANDIDATES FOR CMAS RESISTANT TOP
COATS

by

JUAN JOSE GOMEZ CHAVEZ, B.S. M.E.

THESIS

Presented to the Faculty of the Graduate School of

The University of Texas at El Paso

in Partial Fulfillment

of the Requirements

for the Degree of

MASTER OF SCIENCE

Department of Mechanical Engineering

THE UNIVERSITY OF TEXAS AT EL PASO

May 2016

Acknowledgements

I want to express my most sincere gratitude to all the individuals who have contributed to the completion of this thesis project. First, to my advisor Dr. Ramana Chintalapalle who gave me the opportunity to work in this fascinating project and provided guidance and support during all this learning process. Second, to my project supervisor Dr. Ravisankar Naraparaju who also was a key individual in making this project possible and guided me during my 6 month research term at DLR. I would like to thank Drs. Uwe Schulz and Peter Mechnich for their shared expertise and critical input to this project.

Abstract

State of the art thermal barrier coatings (TBC) commonly made of 7-8 wt. % yttria stabilized zirconia (7YSZ) are used in modern gas turbines to generate a thermal protection to the underlying super alloy components. TBCs allow higher operating temperatures for hot gas path components, thus, generating higher engine efficiency. The infiltration of molten glassy mineral deposits composed of CaO-MgO-Al₂O₃-SiO₂ (CMAS) represents one of the major threats in reducing performance and service life in aero and land based gas turbine engines. The CMAS deposits are ingested into the engine carried commonly in sand, runways debris, fly ash and volcanic ash. The ingested particles melt on the engine's hot gas path components infiltrating the porous TBC, this infiltration generates detrimental effects on the coating such as microstructural degradation and strain tolerance reduction. The present work studied in detail the CMAS infiltration resistance of EB-PVD –yttria (Y₂O₃) coatings which can be used as a top coat on standard 7YSZ TBC layer. Studies were made with Y₂O₃ rich ZrO₂ coatings with an yttria content ranging in 65 wt. % (rest is zirconia). CMAS infiltration experiments were performed at 1250 °C -at time intervals from 1 to 20 hours for long term infiltration and 5 minutes for rapid infiltration using real volcanic ash and a model CMAS source for results comparison. The results show that the studied yttria coatings induced the crystallization of the CMAS melt by forming stable oxyapatite and garnet phases. These layers exhibit a minimal growth making yttria rich coatings promising candidates for CMAS resistant multilayer TBCs. The results also proved a dependency of coating microstructure for infiltration resistance suggesting that the infiltration resistance can be further improved by refining the TBC microstructure by maintaining a densified morphology.

Table of Contents

Acknowledgements.....	v
Abstract.....	vi
Table of Contents.....	vii
List of Tables.....	ix
List of Figures.....	x
Chapter 1: Introduction.....	1
1.1 Problem Statement.....	3
1.2 Significance.....	4
1.3 Objectives.....	5
Chapter 2: Literature Review.....	6
2.1 Thermal Barrier Coating System.....	6
2.2 Y ₂ O ₃ -ZrO ₂ System.....	8
2.3 Calcium-Magnesium-Alumino-Silicates (CMAS).....	10
2.4 CMAS Mitigation Approaches.....	13
2.5 Infiltration Kinetics.....	14
Chapter 3: Experimental Procedure.....	20
3.1 CMAS/VA Powders Collection and Preparation.....	20
3.2 DSC Analysis for CMAS Powders.....	20
3.3 EB-PVD Sample Preparation.....	21
3.4 X-Ray Diffraction Studies.....	21
3.5 CMAS Short Term Infiltration for Standard 7YSZ Coatings.....	22
3.6 CMAS Infiltration Tests for Yttria Rich (YSZ) Coatings.....	23
3.7 Characterization Procedure for Infiltrated Samples.....	24
Chapter 4: Experimental Results.....	25
4.1 DSC Profiles for CMAS and Volcanic Ash Powders.....	25
4.2 XRD Results for CMAS/VA.....	26
4.3 Short Term Infiltration Tests in Standard 7YSZ Coatings.....	26
4.4 XRD Results for CMAS/VA-Yttria Mixtures.....	28

4.5	CMAS Short Term infiltration Test on Yttria Rich Coatings.....	30
4.6	Long Term infiltration on Yttria Rich Coatings at 1250°C.....	36
4.7	Long Term Infiltration for 1225°C.....	44
4.8	Infiltration Kinetics Analysis.....	47
Chapter 5: Discussion		52
5.1	Infiltration Depth Analysis for High Yttria Coatings.	52
5.2	Reaction Layer Growth of Yttria Rich Coatings.	53
5.3	Temperature Dependency Analysis.	59
Chapter 6: Conclusions		63
Works Cited		65
Appendix.....		68
Vita.....		70

List of Tables

Table 3.1: Summary for CMAS/VA powders.	20
Table: 4.5.1: Summary of reaction products for CMAS 1.....	33
Table 4.5.2: Composition of identified phases from Japan ash reaction zone.....	34
Table 4.4.3: Composition of reaction phases of Iceland ash reaction zone.....	35
Table 4.6.1: Summary of reaction products for CMAS 1 1h. 1250°C infiltration.	39
Table 4.6.2: Summary of reaction products for Japan VA 1250°C 1 h. isothermal.	41
Table 4.6.3: Summary of reaction products for Iceland VA.....	42
Table 4.7.1: Reaction products summary for CMAS 1 after 10 h. thermal exposure.	45
Table 4.7.2: Summary of reaction products for Japan VA.	46
Table 4.7.3: Summary of reaction products for Iceland VA.....	47
Table 4.8.3: Calculated times of infiltration for CMAS 1 at 1250°C.	51
Table 5.1: Summary of reaction products at infiltrated columnar gaps for 1250°C.....	53
Table 5.2.1: Summary of reaction products for CMAS 1 at 1250°C.....	55
Table 5.2.2: Summary of reaction products for Japan VA at 1250°C.....	57
Table 5.2.3: Summary of reaction products for Iceland VA.....	59

List of Figures

Figure 1: Typical TBC structures achieved by (a) APS and (b) EB-PVD techniques [17].....	3
Figure 1.1: Proposed multilayered CMAS resistant TBC system based on EB-PVD.....	4
Figure 2.1.1: Section view of Engine Alliance GP7200 aircraft engine, image of a high pressure turbine blade with TBC, and scanning electron microscope (SEM) image of a cross-section view of a standard 7YSZ coated TBC system [2].	7
Figure 2.2: (a) Thermal conductivity of various oxide materials (b) Phase diagram of ZrO ₂ -Y ₂ O ₃ system [17].	9
Figure 2.2.1: Thermal conductivity vs. yttria content in TBCs [10].....	10
Figure 2.3.3: CMAS thermo-mechanical attack driven by capillary forces. The area in red bars shows the inter columnar CMAS infiltration and arrows show direction of CMAS flow.	12
Figure 2.3.4: Schematic illustration of CMAS thermo-chemical attack on standard 7YSZ coatings [34].	13
Figure 2.3.3: CMAS mitigation approaches by (a) Gd zirconate using EB-PVD [37] and (b) Al ₂ O ₃ +TiO ₂ doped 7YSZ using APS [36].	14
Figure 2.5: Schematic for concentric pipe model where (a) represents the top view of the concentric pipe with a kernel (TBC column) inside and (b) shows the area available for CMAS infiltration (columnar gaps shaded in black).	16
Figure 2.5.2: CMAS infiltration schematic on EB-PVD TBCs (a) SEM cross-section view, (b) simplified schematic showing the effect of feather arm length in splitting the flow path.	18
Figure 2.5.3: Contact angle measurement for infiltrating fluids [40].	19
Figure 3.3: (a) EB-PVD coating system schematic, (b) cross-sectional view for the obtained microstructure	21
Figure 3.5a: Sample appearance before and after infiltration.	23
Figure 3.5b: Thermal profile of the furnace and sample for short term infiltration tests.	23
Figure 4.1: DSC profiles for CMAS 1 (black), Japan VA (red) and Iceland VA (blue).	26
Figure 4.3a: Silicon elemental mapping for infiltration determination for Iceland (a), Japan (b) and CMAS1(c) for 0.5 min. infiltration at 1250°C.	27
Figure 4.3b: Infiltration progression for CMAS/VA on 7YSZ samples at 1250°C for different times.	28
Figure 4.4: XRD patterns of CMAS/VA + 65% yttria rich zirconia-mixtures at 1250°C after 10 h.....	30
Figure 4.5a: Infiltrated zone image for (a) CMAS 1, (b) Japan VA and (c) Iceland VA after 5 min. infiltration at 1250°C.	31
Figure 4.5b: High magnification image for the reaction layer at the coating/glass interphase for (a) CMAS 1, (b) Japan VA and (c) Iceland VA.	31
Figure 4.5.1: (a) CMAS1 reaction layer showing crystallization of the glass. (b) Higher magnification view for the label + product from figure (a).	32
Figure 4.5.2: VA/yttria rich zirconia reaction zone showing the crystallization of the glass into a columnar gap sealing product.	34
Figure 4.4.3: Reaction zone for Iceland ash showing the crystallization of the glass.	35
Figure 4.6a: Infiltration measurement for Iceland ash after 20 h. isothermal test at 1250°C. (a) SEM cross sectional view, (b) EDS elemental mapping for Si. Yellow arrows exhibit deep infiltration in large columnar gaps.	36
Figure 4.6b: Infiltration depth progression over time for thermal tests at 1250°C.	37

Figure 4.6.1a: Elemental mapping for CMAS 1 reaction zone after 1 h. 1250°C infiltration.....	38
Figure 4.6.1b: Reaction zone progression for CMAS 1 at 1250°C.	39
Figure 4.6.2a: Reaction layer for Japan VA with elemental mapping at 1250°C test after 1 h....	40
Figure 4.6.2b: Reaction layer progression for Japan VA at 1250°C.	41
Figure 4.6.3a: Reaction layer for Iceland VA at 1250°C after 1 h. with elemental mapping.....	42
Figure 4.5.1b: Reaction zone progression for Iceland VA at 1250°C thermal tests.....	43
Figure 4.7.1: Reaction layer formation for CMAS 1 after 10 h. thermal exposure at (a) 1225°C and (b) 1250°C.	44
Figure 4.7.2: Reaction layer for Japan VA after 10 h. infiltration at (a) 1225 and (b) 1250°C....	45
Figure 4.7.3: Reaction layer for Iceland VA after 10 h. infiltration at (a) 1225°C and (b) 1250°C.	47
Figure 4.8.1: Calculated viscosity for CMAS/VA.....	49
Figure 4.8.2: Permeability of single pipe vs. concentric pipe model.....	50
Figure 5.2.1: Reaction layer schematic for CMAS 1 at 1250°C.....	54
Figure 5.2.2: Reaction layer schematic for Japan VA at 1250°C.	56
Figure 5.2.3: Reaction layer schematic for Iceland VA at 1250°C.	58
Figure 5.3: Reaction layer of Iceland VA at (a) 1225 and (b) 1250°C after 10 h. infiltration.	60
Figure 5.3.1: Infiltration depth for CMAS/VA for 10 h. infiltration tests.....	61
Figure 5.3.2: Reaction layer growth for CMAS/VA after 10 h. infiltration for 1225 and 1250°C.	62

Chapter 1: Introduction

State of the art thermal barrier coatings (TBCs) are used in hot gas path components for modern gas turbine engines to enable them to operate at higher temperatures by providing a thermal insulation to the underlying metallic components, thus increasing the thermodynamic efficiency of the engine [1, 2]. By deposition of a low thermal conductivity ceramic top coat (100-500 μm thick) on the superalloy component, gas turbines are able to operate at temperatures higher than the melting point of superalloys ($\sim 1300^\circ\text{C}$) [3].

The common TBC system is formed by a combination of 2 grown layers deposited on top of a superalloy substrate. The first layer is a metallic bond coat layer (BC) commonly made of MCrAlY (M=Ni, Co and combinations) and performing 2 main functions [4]:

- i) To protect the substrate from oxidation and hot corrosion by growing a thin oxide layer (1 to 10 μm) of Al_2O_3 during service. The oxide layer is commonly referred as thermally grown oxide (TGO).
- ii) To provide the required adhesion between the substrate and the outer ceramic layer.

Additionally, the TGO generated during service has to be highly heat resistant and should not experience considerable plastic strain since it leads to TBC spallation.

The second layer is the TBC itself commonly made of 7-8 wt.% Y_2O_3 stabilized ZrO_2 (7YSZ) which is used for thermal insulation. The combination of porosity of the TBC material and its very low thermal conductivity provides the properties for an excellent high temperature insulator [5]. Additionally, significant research efforts have been performed in order to find substitute materials for commonly used 7YSZ, some of the proposed materials for next generation TBCs involve $\text{Gd}_2\text{Zr}_2\text{O}_7$, $\text{La}_2\text{Zr}_2\text{O}_7$, among others [6, 7, 8, 9]. The common deposition techniques for TBCs include electron beam physical vapor deposition (EB-PVD) and air plasma spray (APS). Different coating structures are achieved with each deposition technique. A network of porous columns is achieved by varying the deposition parameters in EB-PVD, whereas for APS technique, a system of porous layers with micro-cracks stacked on top of each

other is achieved by the variation of deposition techniques and post deposition heat treatment. A common 7YSZ TBC deposited structure is shown in **Figure 1.1** for each deposition technique described above. Furthermore, the service life of the TBC not only depends on the chemical composition, it also depends on the porous structure and the adhesive strength of the ceramic layer which depend directly on the deposition technique [4]. The columnar gaps formed on the coatings grown by EB-PVD technique offer a higher strain tolerance and thermal shock resistance upon heating/cooling cycles, but they lead to a lower thermal conductivity as for their counterpart TBCs grown by APS technique [10].

The main limitations of standard 7YSZ TBCs are due to the loss of adhesive strength of the bond coat caused by oxidation and formation of the TGO resulting in TBC spallation, and the infiltration of impurities (Vanadium, Sulphur and mineral particles) into the ceramic top coats. This infiltration is responsible for hot corrosion and phase transformation of ZrO_2 which generates loss of mechanical properties such as thermal conductivity and plastic strain tolerance. Moreover, the increasing demand for higher operating temperatures in aero-derivative and land-based gas turbines has brought into attention the effects of infiltrated mineral deposits into hot engine's components. The siliceous mineral deposits commonly consisting on $CaO-MgO-Al_2O_3-SiO_2$ (CMAS) are ingested as sand, runway debris, volcanic ash and fly ash. The CMAS particles deposit on the hot gas path components and melt generating infiltration into the porous TBC structure (regardless of the deposition technique used) resulting in premature failure due to microstructure degradation, sintering and spallation. The molten CMAS infiltrates the columnar gaps, pores and cracks flowing inwards the TBC and hardens as it flows down the thermal gradient. The hardening of the CMAS compound generates a stiffening of the TBC which is no longer able to sustain plastic strain due to the total block of the TBC porosity generating delamination [11, 12]. Subsequently, the interaction of the CMAS melt with the TBC at high temperatures generates a thermo-chemical damage system characterized by the dissolution of the initial metastable tetragonal (t') YSZ due to the depletion of Y_2O_3 phase and re-precipitation of Zr with a composition and structure that depends on the CMAS chemistry [12, 13]. Due to the

serious effects that CMAS attack has on reducing the service life of YSZ TBCs, research efforts have increased in proposing methods for CMAS infiltration resistance. Some of the methods proposed include the utilization of overlaying coatings on top of the YSZ in arresting the CMAS infiltration [14, 15]. Another method proposes the addition of dopants to the original top ceramic coats to generate reactant products that accelerate the crystallization of molten CMAS sealing any further infiltration [16].

The focus of this research work was to study the CMAS infiltration kinetics in standard 7YSZ coatings in detail and propose a physical model. Subsequently, yttria rich-zirconia based coatings were proposed as CMAS resistant coatings and coated by varying the Y_2O_3 contents in YSZ ranging from 35 wt. % to 70 wt. % (rest amounts belong to ZrO_2). The infiltration behavior of these coatings was tested isothermally at temperatures of 1225°C and 1250°C – within the intervals of 2 to 5min for rapid infiltration analysis and 1 to 20 hours for long term using real volcanic ash and a model CMAS source. The infiltration resistance of the developed coatings is discussed for their potential selection for CMAS resistant multilayer systems.

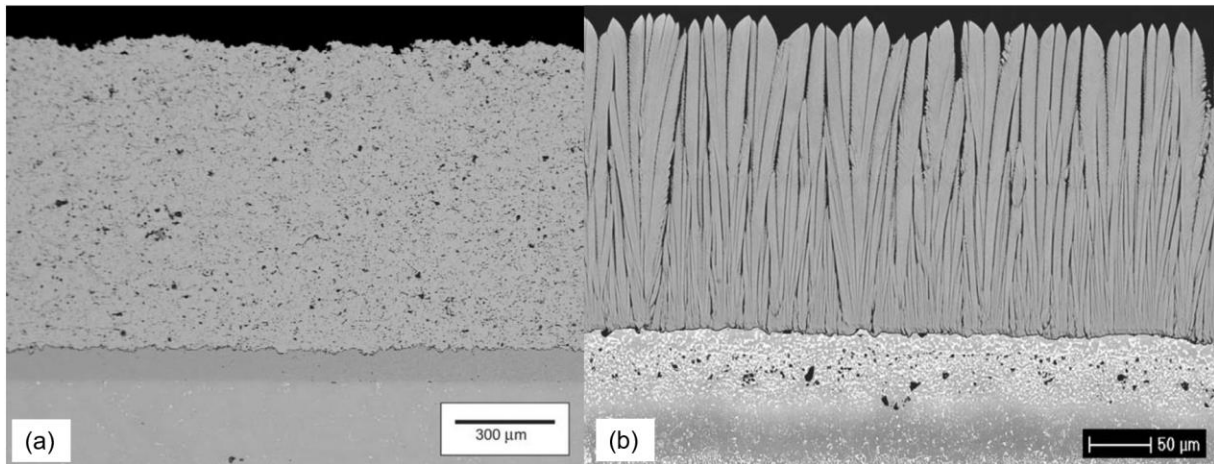


Figure 1: Typical TBC structures achieved by (a) APS and (b) EB-PVD techniques [17].

1.1 Problem Statement

The need for more efficient gas turbine engines has generated a large influence on pushing for higher engine operating temperatures. At higher temperatures the problem of hot

corrosion due to engine ingestion of siliceous minerals generates a big concern for aviation and industrial gas turbines. Hence, there is a critical demand for TBC systems that enable higher operating temperatures with high reliability. The goal of this project is to develop CMAS resistant EB-PVD TBC top coat based on YSZ with higher yttria contents (>50 wt.%). A new multilayer TBC structure can be developed keeping the standard 7YSZ layer as a base layer for thermal protection and a top -sacrificial CMAS resistant layer as shown in **Figure 1.1**.

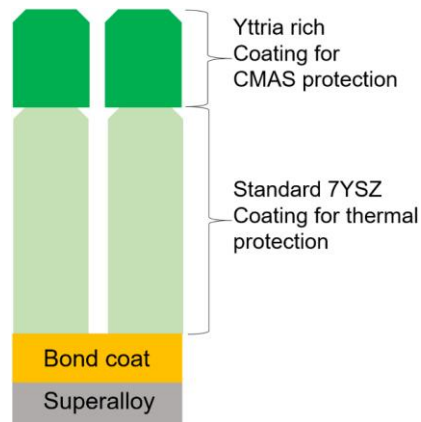


Figure 1.1: Proposed multilayered CMAS resistant TBC system based on EB-PVD.

1.2 Significance

Due to the eruption of the Eyjafjallajökull volcano located in Iceland on 2010, the safety regulations for the aviation industry had to be reconsidered due to the large widespread of the volcanic ash cloud generating a substantial economic loss due to the extended air space closure [18]. Due to this event, a higher pressure has been put on aircraft engine manufacturers to effectively address this volcanic ash (VA) attack issue and reduce economical losses for future events. High yttria based coats show a potential for CMAS arrest in TBC systems [16, 19, 20, 21]. However, there is no available literature for infiltration tests using real volcanic ash on EB-PVD yttria rich coatings. Thus, a better understanding of VA with –high yttria coatings interaction at high temperature can lead to significant benefits in the performance and lifetime extension for aero-derivative and land based gas turbine engines.

1.3 Objectives

The objectives of this work are the following:

1. To gain a better understanding in the CMAS infiltration kinetics on standard 7YSZ EB-PVD coatings.
2. Develop a mathematical standardized model for CMAS infiltration prediction based on the fluid properties (viscosity, surface tension) and the microstructural properties of the TBC (permeability, pore connectivity)
3. Test and evaluate CMAS resistant top coat candidates based on high yttria (Y_2O_3) contents (65 wt. %) for future multilayer CMAS/VA resistant TBCs.

Chapter 2: Literature Review

2.1 Thermal Barrier Coating System

2.1.1 Ceramic Top Coat or TBC

The ceramic top coat or thermal barrier coating (TBC) represents the highly heat insulative ceramic top coat applied commonly by APS or EB-PVD techniques to the top surfaces of metallic engine parts in the hot gas path section of the engine. Besides thermal insulation for the metallic components, the TBCs must possess a high strain-compliance to minimize thermal cyclic stresses due to the thermal expansion mismatch with the superalloy material, and must reflect a significant amount of the radiant heat coming from the hot gases [2]. In addition, TBCs must be able to maintain thermal protection during prolonged thermal cycles and service times pushing the material to work under extreme thermal gradients ($1^{\circ}\text{C } \mu\text{m}^{-1}$) and energy fluxes (1 MW m^{-1}) without separating from the engine parts [2]. The main factors that allow TBCs to operate reliably under all these operating conditions are the following: (1) The TBC processing technique (APS or EB-PVD) which incorporates a high porosity (about 15%) due to its high deposition rate therefore allowing a high strain compliance and reduced thermal conductivity [2, 4], (2) the mechanical robustness of all the TBC system generated by the combination of the deposited layers and grown oxides (will be explained in the following sections) as shown in **Figure 2.1.1**, and (3) the commonly used 7 wt.% YSZ for TBCs which provides all the required thermal properties and a relatively good fracture toughness due to a specific toughening mechanism [22].

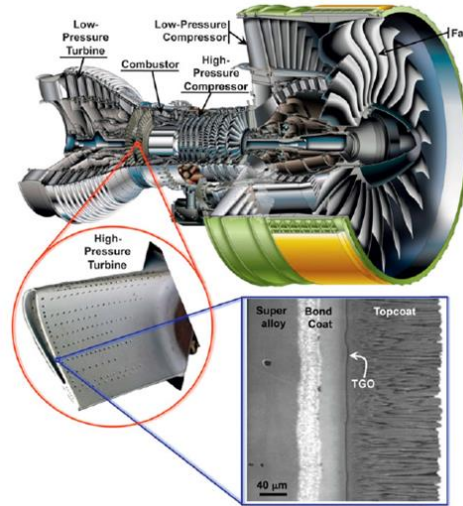


Figure 2.1.1: Section view of Engine Alliance GP7200 aircraft engine, image of a high pressure turbine blade with TBC, and scanning electron microscope (SEM) image of a cross-section view of a standard 7YSZ coated TBC system [2].

2.1.2 Bond Coat

The typical TBC system is composed by two deposited layers, the ceramic topcoat which provides thermal insulation and the bond coat responsible to provide the adhesive strength for the ceramic coat with the superalloy substrate and oxidation resistance for the metallic substrate.

The typical bond coat material used in state of the art YSZ TBCs is MCrAlY where M is nickel and cobalt [5]. In order to provide oxidation resistance, the bond coat has to grow an oxide protective scale during service. The oxide protective scale formed is commonly composed by α -Al₂O₃. The bond strength provided by the bond coat is generated by the thermal expansion coefficient matching between top coat and substrate materials and by the rough surface finish generated with the deposition technique. The matching of thermal expansion coefficients reduces the amount of plastic strain generated at the interface of the top coat/bond coat upon thermal cycling [23]. In addition, bond coats have to be chemically homogeneous, devoid of segregants and creep/yield resistant.

2.1.3 Thermally Grown Oxide (TGO)

The TGO represents an arguable layer in the TBC system due to the facts that it has a major influence on TBC durability but it also represents a common TBC failure point. Due to the porosity of the ceramic top layer, the TBC system has a high oxygen permeability which at high temperatures it can lead to premature failure due to hot oxidation of the metallic components. In order to generate oxidation resistance to the underlying metallic components, the bond coat grows a TGO protective scale during service. The design of the bond coat is meant to act as a local Al reservoir, enabling α -Alumina to be formed during oxides/bond coat interaction. Alumina represents a preferred oxide because of its low oxygen diffusivity and superior adherence [24]. In contrast, TBCs' failure mechanism such as delamination/spallation is commonly generated or started at the TGO/bond coat or TGO/TBC interfaces [25].

2.2 Y_2O_3 - ZrO_2 System

Ceramic materials are well known for possessing a low thermal conductivity and coefficient of thermal expansion which make them suitable for high temperature applications. Zirconia (ZrO_2) is commonly used as a base ceramic material for TBC applications due to its low thermal conductivity which has no significant temperature dependency compared with other oxides as shown in **Figure 2.2a**. Furthermore, one of the main characteristics of zirconia is its polymorph solid nature from which three phases are known: Monoclinic (m) $<1170^\circ C$, tetragonal (t) $1170-2370^\circ C$ and cubic (c) $>2370^\circ C$ [4]. The presence of different phases (monoclinic and tetragonal) at critical operational temperatures generates a disadvantage in the service life of the ZrO_2 based TBCs due to the fact that (t) phase is reversibly transformable to the (m) phase during thermal cycling. During this transformation, a crystal lattice volume change happens generating a volume increase from 3% to 12% which leads to micro cracking and subsequent TBC spallation [26]. Additionally, the phase transformation in zirconia can be suppressed making oxide additions to form solid solutions of fluorite crystalline structure with zirconia [4]. Some of the oxide stabilizers for zirconia are as follows: CaO, MgO, Y_2O_3 and

Yb_2O_3 . Among the mentioned zirconia stabilizers, yttria (Y_2O_3) forms the most stable solid solution for a ceramic top coat base material.

The phase stability generated by yttria additions to the zirconia ceramic has been the material of choice for modern state of the art TBCs. The common ceramic composition used in TBCs is made of 7 % wt. yttria stabilized zirconia (YSZ). It was found that this is the limiting composition to form the metastable ‘non transformable’ tetragonal zirconia phase (t') when the ceramic is quenched from the cubic phase field as shown in **figure 2.2b**. This phase avoids the tetragonal to monoclinic phase change which generates a poor thermal cycling resistance due to TBC spallation [17]. This t' phase shows excellent thermal stability at temperatures up to 1200°C, but at higher temperatures it suffers from sintering effects at extended temperature exposures, a phase transformation from t' to cubic and tetragonal [27], and CMAS attack.

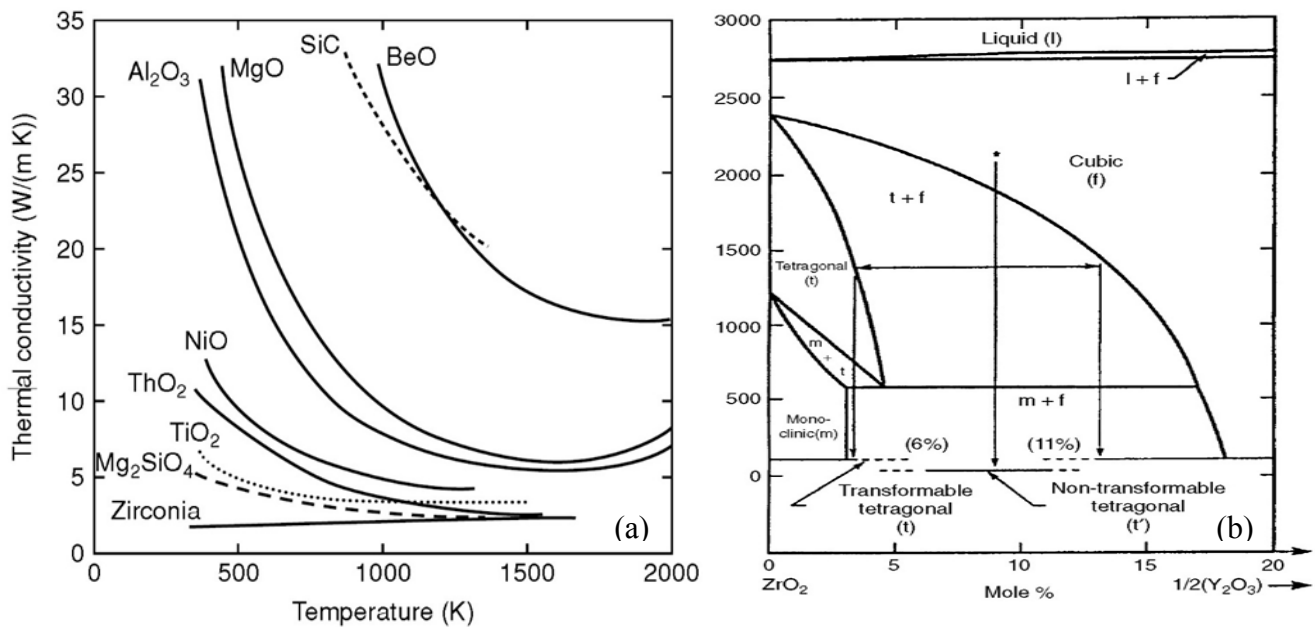


Figure 2.2: (a) Thermal conductivity of various oxide materials (b) Phase diagram of ZrO_2 - Y_2O_3 system [17].

2.2.1 Y₂O₃ Effects in Overall TBC Properties

The addition of yttria to the YSZ system generates a reduction in the thermal conductivity of the TBC due to a shortage in the intrinsic mean path in zirconia by increasing phonon dispersion [10]. **Figure 2.1.1** shows a comparison in the reduction of thermal conductivity in TBCs by the addition of yttria. It can be seen how for EB-PVD systems as the amounts of yttria are increased (up to 20 wt. %), the thermal conductivity is significantly reduced compared to standard 7YSZ (7 wt. %). Additionally, the high yttria composition in YSZ TBC systems are claimed to exhibit high sintering resistance [28]. However, it is well known that the addition of yttria to zirconia based coatings carries a significant reduction in the toughness of the TBC. For that reason, yttria rich TBCs exhibit a higher potential in multilayer coating systems were it can serve as a sacrificial oxide layer with 2 main purposes: to provide CMAS infiltration resistance and extra reduction in thermal insulation to the system.

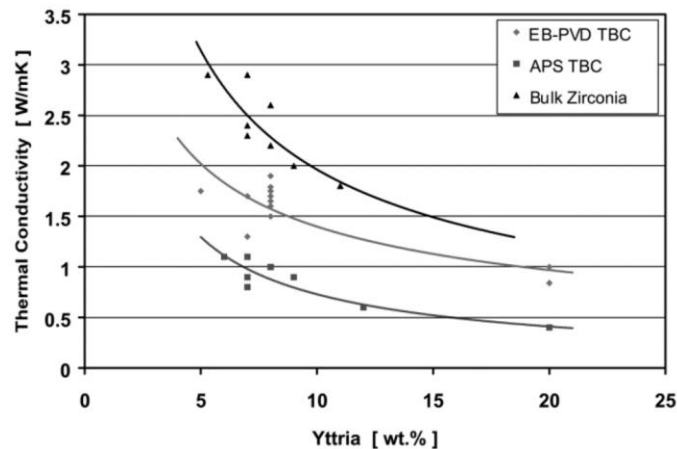


Figure 2.2.1: Thermal conductivity vs. yttria content in TBCs [10].

2.3 Calcium-Magnesium-Alumino-Silicates (CMAS)

CMAS is a form of inorganic glass commonly present in igneous rocks, dust, sand and magmas. One of the important characteristics of CMAS is its common composition through the planet [29]. The presence of these mineral particles in engine components at low temperatures

generate erosive wear in TBCs, whereas molten at high temperatures ($>1150^{\circ}\text{C}$), they generate detrimental thermo-mechanical and thermo-chemical effects in TBCs reducing their service life.

2.3.1 Volcanic Ash

For the past 20 years, volcanic ash has been identified as a threat for aviation making the year of 2010 the turnout point in aviation safety due to the eruption of the Eyjafjallajökull volcano in Iceland. The eruption caused a major disruption in the European air traffic exposing the big threat that large volcano eruptions represent for airspace safety.

Volcanic ash (VA) represents a major threat in CMAS attack for aircraft engines due to its glassy amorphous nature which exhibits a low glass transition temperature ($\leq 900^{\circ}\text{C}$) generating a softening and partial melting of the glass [30]. Thus, at the engine operating temperatures (1200 to 1400°C) the effects of CMAS infiltration should be more aggressive for ingested volcanic ash than for other larger crystalline airborne particles which have in contrast higher melting temperatures (1170°C up to 1700°C) [18, 31].

2.3.3 CMAS Thermo-Mechanical Attack

Modern gas turbines have service temperatures ranging in 1300°C [2]. At engine's operating temperatures, the ingested CMAS particles melt and infiltrate into the porosity and columnar gaps of EB-PVD and APS TBCs under capillary forces. CMAS viscosity, surface tension and additionally TBC permeability represent the main mechanisms governing the CMAS infiltration into the porous TBC structure. As the CMAS starts to melt at high temperatures ($>1100^{\circ}\text{C}$), its lower viscosity no longer sustains the capillary forces therefore, an increased infiltration rate is generated at higher temperatures. Once the CMAS melt flows down the TBC's thermal gradient, its viscosity increases generating a slower infiltration rate and crystallization. The crystallization of the CMAS melt generates stiffening of the TBC structure leading to a loss of strain tolerance during cooling which creates a ceramic coat delamination. Additionally, the partial or total CMAS infiltration generates a significant degradation on the insulating properties of the TBC [32]. At total CMAS infiltration where the CMAS melt infiltrates and reaches the

TGO, a more severe damage is generated. Once the CMAS infiltrated TGO is exposed to thermal cycling, the thermal expansion coefficient (TEC) between the bond coat and the ceramic coat is altered. The TEC mismatch between both layers generates a higher strain rate during cooling leading to TBC spallation [33]. **Figure 2.3.3** shows the mechanism of CMAS thermo-mechanical attack in EB-PVD TBCs driven by capillary forces.

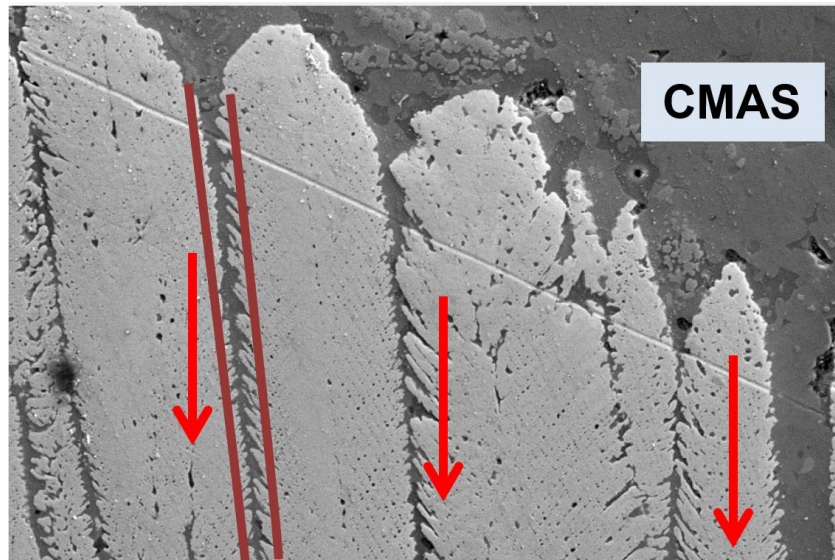


Figure 2.3.3: CMAS thermo-mechanical attack driven by capillary forces. The area in red bars shows the inter columnar CMAS infiltration and arrows show direction of CMAS flow.

2.3.4 CMAS Thermo-Chemical Attack

The increase in gas turbine operating temperatures represents a major factor in improving thermal efficiency. As the demand for higher firing temperatures increases, the standard 7YSZ TBCs will not be able to meet the reliability requirements for temperature ranges above 1200°C due to the t' phase stability and CMAS thermo-chemical attack [34]. Significant research efforts have been concentrated in understanding the chemical reaction between CMAS melts and 7YSZ TBCs. The main mechanism governing the chemical reaction between molten glassy silicates and 7YSZ is due to the dissolution of yttria and re-precipitation with a composition and structure

that depends on the local chemistry of the melt which generates a zirconia phase transformation [12, 35]. **Figure 2.3.4** shows a schematic of the common thermo-chemical reaction system at high temperatures between CMAS and YSZ [34].

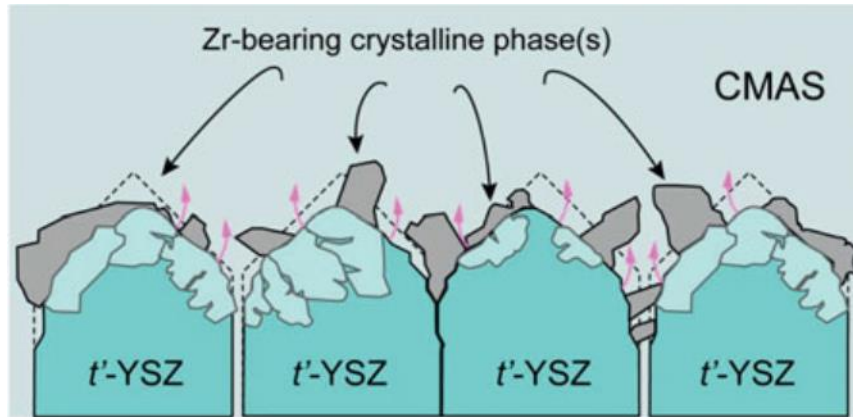


Figure 2.3.4: Schematic illustration of CMAS thermo-chemical attack on standard 7YSZ coatings [34].

2.4 CMAS Mitigation Approaches

As research have demonstrated that the infiltration of CMAS melts on standard 7YSZ TBCs bring detrimental effects on the lifetime of the coatings, numerous other approaches for CMAS arrest have been proposed [15, 36, 37]. Most of the proposed approaches for CMAS mitigation focus on the chemical reaction generated between the CMAS melt and the TBC by mostly following two mitigation procedures: (1) Stop the melt by crystallizing its main constituents (mostly silicates) and therefore, elevating their melting temperature, and (2) to fill the pores and columnar gaps with the new crystalized phases in order to block any excess melt into the TBC [34]. Most of the published literature for CMAS mitigation has been based on $Gd_2Zr_2O_7$ [37] and 7YSZ TBCs doped with Al and Ti as solid solution (ss) [36] as seen in **Figure 2.4**.

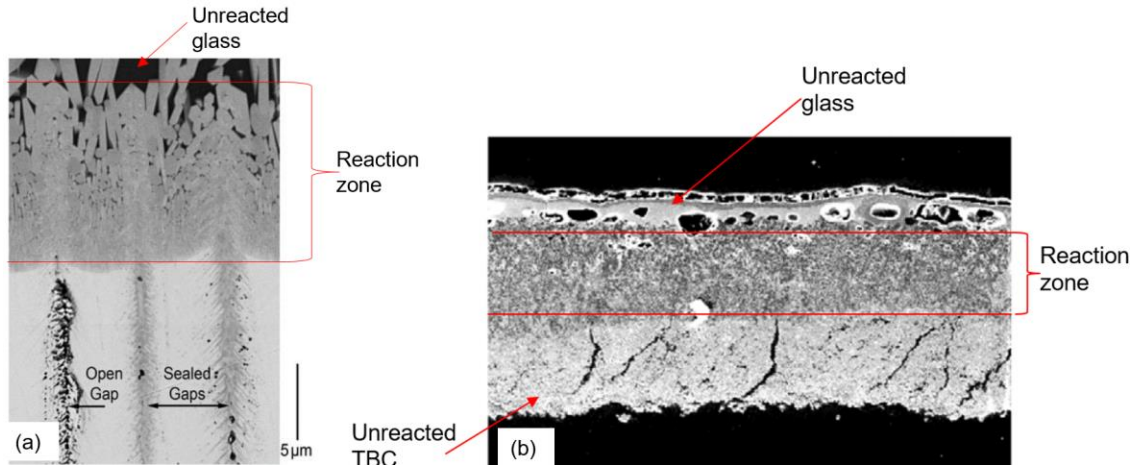


Figure 2.3.3: CMAS mitigation approaches by (a) Gd zirconate using EB-PVD [37] and (b) $\text{Al}_2\text{O}_3+\text{TiO}_2$ doped 7YSZ using APS [36].

2.3.4 Yttria Rich Top Coats for CMAS Mitigation

The use of high Y_2O_3 content top coats for CMAS mitigation has not been extensively researched yet. However, the few available publications in this field have shown promising results as far as effectiveness for CMAS mitigation by using APS and powder analysis [16, 20, 38, 21]. The results report a formation of a metastable Ca-Y-Si oxyapatite phase which acts as main CMAS crystallization product. Additionally, Elis et al. have reported a new formed phase identified as “Garnet” which has exhibited CMAS arrest properties as well [20]. It is also important to emphasize that no results have been published until now with the use of EB-PVD yttria rich coatings for CMAS infiltration studies. All the published literature on yttria rich coatings emphasize on the characterization of the formed reaction products at interface of the molten CMAS glass and the coating.

2.5 Infiltration Kinetics

EB-PVD TBCs are commonly used for high pressure rotating blades due to their highly reliable strain tolerance under extreme thermal gradients and centrifugal forces present in high pressure turbine blades. The strain tolerance is obtained by the developed porous lamellae microstructure with gaps, and feather arms structures formed at the edges of columns. However,

this gaps which provide resistance to thermal shocks are the main cause of infiltration of glassy molten CMAS deposits driven by capillary forces acting during high CMAS wetting on the TBC surface. Some of the main factors governing the infiltration kinetics are the influence of contact angles of the melts with the columnar structure, the viscosity of the melt, surface tension and permeability of the porous medium. The latter is totally dependent on the geometry of the coating and has shown a big influence on the infiltration depth. A study performed by Naraparaju et al. at the German Aerospace Center (DLR) has shown a reduction in CMAS infiltration on 7YSZ TBCs by controlling the microstructure of the coating reducing columnar gaps, incrementing the overall porosity of the coating and feather arms. The results are currently under review and in process for publication.

The infiltration kinetics can be summarized by assuming the open columns of the TBC as small pipes open for infiltration. The wetting of the TBC surface is defined by the contact angle generated between the molten CMAS and the TBC surface which has a value of zero at full wetting ($\text{Cos } \Theta = 1$). By using the standard system for infiltration of liquids into porous medium, it can be summarized that the time required for a fully wetting liquid ($\text{Cos } \Theta = 1$) to infiltrate into a depth of L due to a capillary action into the coating can be expressed as [12, 39]:

$$t = \left[\frac{kt}{8Dc} \left(\frac{1 - \omega}{\omega} \right)^2 L^2 \right] \frac{\eta}{\sigma LV} \quad (1)$$

Where ω is the pore fraction affected by the infiltrated fluid, Dc is the capillary diameter or columnar gap diameter, kt is the tortuosity factor (1-10). η represents the viscosity of the fluid and σLV the surface tension of the fluid.

Furthermore, Naraparaju et al. proposed a new approach for infiltration kinetics where the TBC is no longer considered as a network of single pipes, rather it is considered as a network of concentric pipes with a kernel inside as shown in **Figure 2.5**.

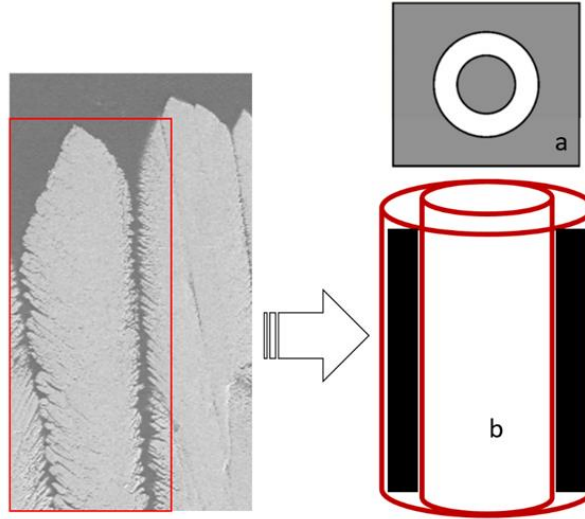


Figure 2.5: Schematic for concentric pipe model where (a) represents the top view of the concentric pipe with a kernel (TBC column) inside and (b) shows the area available for CMAS infiltration (columnar gaps shaded in black).

By using this new approach, the time for CMAS infiltration can be calculated by the following equation [Naraparaju et al.]:

$$t = \frac{\mu r h^2}{2\sigma \cos\theta k} \quad (2)$$

Where μ represents the viscosity of the fluid, r represents the new radius coming from the area exposed for infiltration, h the height of infiltration, σ the surface tension of the fluid, θ the contact angle of the molten liquid with the surface and k the permeability of the TBC.

The new radius value for the infiltration can be calculated from the new surface area susceptible for CMAS infiltration as show in equation 3.

$$r = \sqrt{r_b - r_a} \quad (3)$$

Where r_b represents the pipe radius and r_a the TBC column radius (kernel).

2.5.1 TBC Permeability

The permeability of the medium represents a factor that defines the speed of infiltration of a fluid through a porous medium. It is influenced by several factors such as pore fraction, tortuosity, and pore dimensions and distribution. The model is extended in terms of the pipe radius “b” and the kernel (TBC column) radius “a”. The new permeability equation is expressed as follows [Naraparaju et al.]:

$$k = \frac{\varphi}{8\tau^2} b^2 \left[1 + \frac{a^2}{b^2} + \left(1 - \frac{a^2}{b^2} \right) \left(\frac{1}{\ln \frac{a}{b}} \right) \right] \quad (4)$$

Where φ represents the pore fraction of the coating and τ the tortuosity factor of the TBC.

2.5.2 Tortuosity

The tortuosity factor represents an important microstructure parameter that influences the CMAS infiltration. It can be described as the ratio of the distance for a fluid to cover a linear length to the actual total length that a fluid has to travel between two points following a certain defined path. This parameter is important for EB-PVD TBCs infiltration analysis since their cross-sectional microstructure have a common feature of lateral porous on the columns called “feather arms”. This “feather-arms” are believed to offer significant help on reducing CMAS infiltration time as presented in Naraparaju et al. studies. Due to their microstructural influence on the tortuosity factor added as the size and amount of feather-arms are increased, the feather-arms act as splitting channels for the fluid path as shown in **figure 2.5.2**.

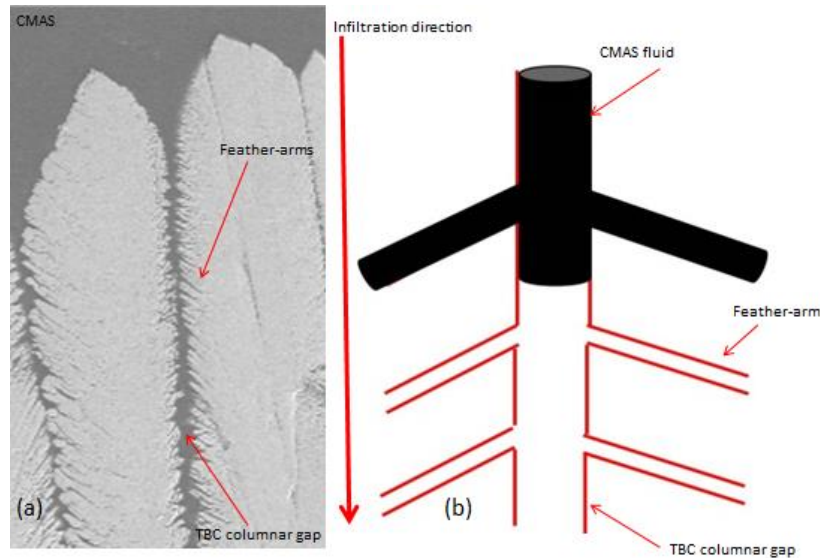


Figure 2.5.2: CMAS infiltration schematic on EB-PVD TBCs (a) SEM cross-section view, (b) simplified schematic showing the effect of feather arm length in splitting the flow path.

2.5.3 Surface Tension of Infiltrated Fluids

Surface tension represents the factor controlling mainly the contact angle of the molten fluid. The contact angles represent an important factor since at high wetting the infiltration takes place. High wetting angles are represented by a contact angle of the fluid ranging from 0 to 90 degrees while low wetting is shown at contact angles between 90 and 150 degrees [40]. Furthermore, contact angles ranging higher than 150 degrees are considered as super hydrophobic surfaces and do not show significance for CMAS infiltration. **Figure 2.5.3** shows a schematic of how the contact angles are measured when a fluid is in contact with a flat surface.

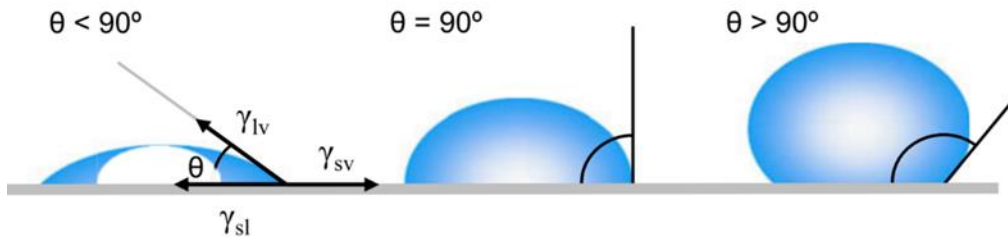


Figure 2.5.3: Contact angle measurement for infiltrating fluids [40].

Additionally, it has been reported from literature an effective way to determine surface tension for silicate glass melts at 1400°C using their chemical composition. The equation is as follows [41]:

$$\sigma_{LV} \left(\frac{mN}{m} \right) = 271.2 - 2.22K_2O + 1.96MgO + 3.34CaO + 2.68FeO + 3.47Al_2O \quad (5)$$

Only the relevant oxides have been included in the equation and all the concentrations are used in mole percent.

2.5.4 Viscosity of Infiltrated Fluids

Viscosity plays also an important role in the infiltration kinetics of CMAS melts since it is the main force restricting the liquid flow. Viscosities can also be estimated from the chemical composition of the CMAS melt described by Giordano et al. [42]. However, recent results performed by Naraparaju et al. have shown a significant discrepancy between experimentally measured viscosities on CMAS carrying powders and estimated values by the Giordano model.

Chapter 3: Experimental Procedure

3.1 CMAS/VA Powders Collection and Preparation

One model-CMAS and two natural volcanic ash powders were used in this study. The natural volcanic ashes which were collected from site correspond to the ones ejected from the volcanos located in Iceland (Eyjafjallajökull) and southern Japan (Sakurajima). The synthesized CMAS powder (CMAS 1) has been used extensively by DLR studies, its chemical composition was selected from performed screenings on real aircraft engines operated on sandy environments [43, 44]. The production methods are described elsewhere [45, 44]. **Table 3.1** shows the chemical composition of the used powders. The chemical compositions of the volcanic ashes show a significant difference in their composition especially in silica (SiO_2), FeO_2 and TiO_2 content, which states that different volcanos exhibit different chemical compositions.

Table 3.1: Summary for CMAS/VA powders.

Label	Chemical composition (Mol. %)								Crystalline Phase	Melting point
	SiO_2	CaO	MgO	Al_2O_3	FeO	TiO_2	Na ₂ O	K ₂ O		
CMAS 1	41.7	24.7	12.4	11.1	8.7	1.6	0.0	0.0	Pyroxene - Anorthite	1250 °C
Japan ash	66.3	11.4	0.3	15.7	1.4	0.0	4.3	0.7	Anorthite - Amorphous	1170 °C
Iceland ash	49.7	12.5	6.1	7.4	17.6	4.3	2.0	0.4	Amorphous	1150 °C

3.2 DSC Analysis for CMAS Powders

Differential Scanning Calorimetry (DSC) measurements were performed on the CMAS/VA powders between room temperature and 1300°C in a STA 449 F3 Jupiter (Netzsch, Selb, Germany) in order to determine important temperature ranges (melting point, glass transition temperature, etc.) and effects to the melting behavior by the presence of crystalline phases in the used CMAS powders.

3.3 EB-PVD Sample Preparation

YSZ with a high yttria (Y_2O_3) content samples were produced by using EB-PVD equipment with a maximum beam power of 150 KW. Evaporation was performed by a jumping beam on dual evaporation sources namely 7YSZ-(source 1) and 100 wt.% Y_2O_3 (source 2) as shown in **Figure 3.3(a)**. By using this deposition set up, the yttria content varied with respect of the location to the evaporation source meaning the closer the sample to the 7YSZ ingot, the lower the yttria composition in the coating. The samples were deposited on plane Alumina (Al_2O_3) substrates. The use of Alumina substrates allows the long time infiltration test at 1250°C temperatures without generating any damage to the substrate since nickel based super alloys have melting points close to this testing temperature. Additionally, it allows to see a simulation effect for the case when the CMAS melt reaches and reacts with the TGO. The obtained samples had a thickness of 120-160 microns and a chemical composition of 35 wt.% to 65wt. % yttria. **Figure 3.3(b)** shows the obtained microstructures for the as deposited samples.

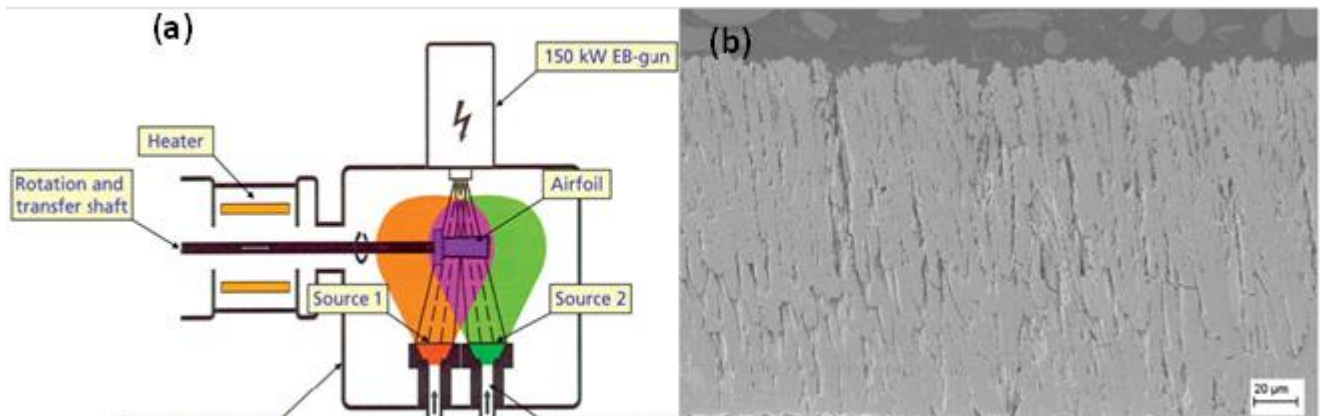


Figure 3.3: (a) EB-PVD coating system schematic, (b) cross-sectional view for the obtained microstructure

3.4 X-Ray Diffraction Studies

CMAS-yttria rich zirconia-powder mixture was prepared with a 60 wt. % composition of CMAS bearing powder and 40 wt. % of yttria rich powder (65 wt. %) obtained from the as coated samples. The powder mixture was then heat treated for 10 h. at 1250°C and furnace

cooled. After heat treatment, the molten mixture was crushed in mortar for 30 min. to make it fine powder facilitating handling for XRD studies. XRD analyses were performed using Si single crystal holders in a Siemens D5000 diffractometer using $\text{CuK}\alpha$ radiation with a secondary graphite monochromator (EVA/Topas 4.2 software package, Bruker AXS, Karlsruhe, Germany).

3.5 CMAS Short Term Infiltration for Standard 7YSZ Coatings

Standard EB-PVD 7YSZ coatings of 425 μm thickness were used for rapid CMAS infiltration studies. The infiltration studies were performed in a thermal cyclic furnace at 1250°C for infiltration times of 0.5, 2 and 5 min. CMAS was applied in the amount of 20 mg/cm^2 on top of the samples. **Figure 3.5a** shows the sample appearance before and after infiltration.

The cyclic furnace was calibrated by preheating the loading chamber to 1250°C for 1 h. before placing the samples on it. The sample temperature was measured with a thermocouple placed next to the surface of the coating during the heating process. After the 1 h. preheating of the loading chamber, the samples were loaded into the furnace and the heating profile was measured as shown in **Figure 3.5b**. The heating profile shows an overall time of 480 sec. (8 min.) \pm 15 sec. for the sample to reach 1250°C. The heating time was set for 13 min. (780 sec.) after sample loading which provides a constant temperature of 1250°C for 5 min.

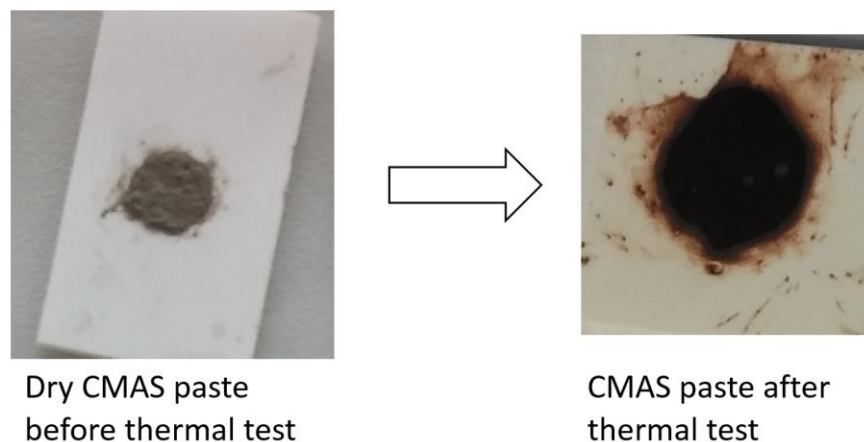


Figure 3.5a: Sample appearance before and after infiltration.

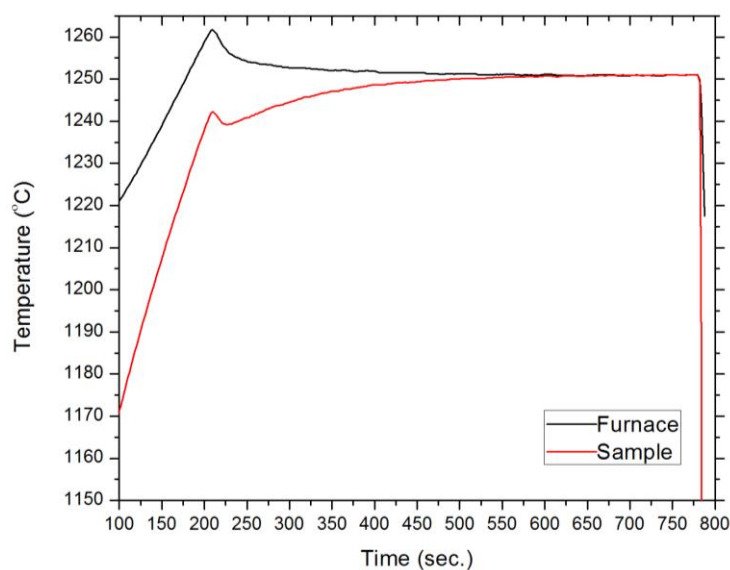


Figure 3.5b: Thermal profile of the furnace and sample for short term infiltration tests.

3.6 CMAS Infiltration Tests for Yttria Rich (YSZ) Coatings

CMAS long term infiltration experiments for yttria rich coatings were conducted isothermally at temperatures of 1225 and 1250°C in a chamber furnace using a CMAS amount of 20 mg/cm². The times of infiltration were varied between 1 to 20h. Short term infiltration tests were performed at 1250°C for 5 min. using the technique described in the previous section.

3.7 Characterization Procedure for Infiltrated Samples

Standard metallographic techniques were used for sample preparation in the cross-section analysis. Scanning Electron Microscopy (SEM) (DSM ultra 55, Carl Zeiss NTS, Wetzlar, Germany) techniques were performed using a system equipped with an energy-dispersive spectroscopy (EDS) (Inca, Oxford Instruments, Abingdon, UK) to study and characterize the reacted zones and infiltration depths. The infiltration depths were confirmed by EDS elemental mapping and spot analysis.

Chapter 4: Experimental Results

4.1 DSC Profiles for CMAS and Volcanic Ash Powders

Figure 4.1 shows the obtained DSC graphs for CMAS/VA powders. The DSC results for all the CMAS composition used are plotted for the thermal range of 500 to 1300°C. For the CMAS 1 composition, the endothermic sharp peak shown in the range of 1225 to 1260°C represents the melting process. The linear transition of the DSC curve for the CMAS 1 powder confirms the crystal nature of the phases present in the powder mixture.

The VAs exhibit a very different DSC curve profile compared to the obtained from CMAS 1. The non-linear behavior for the volcanic ashes confirms the amorphous nature of their constituents. For the Iceland two small broad exothermic peaks are observed from 840 to 910°C and from 1020 to 1050°C suggesting partial crystallization of the glass constituents. After the second exothermic peak a significant endothermic peak is observed for a large temperature range from about 1060 to 1150°C which suggest the melting range of the glass.

The Japan VA does not exhibit significant endothermic peak suggesting no specific melting point for the glassy phases. One large depression in the curve is shown at a large area from 700 to 900°C which could be attributed to the glass transition temperature. After that, a small exothermic peak is observed forming at 1050°C followed by what seems to look as a formation of an endothermic peak from the range of 1100 to 1175°C which might suggest the melting point of the glass.

It is important to note that the crystalline nature of the CMAS 1 generates the narrowest melting range (1225 to 1250°C) and highest melting point (about 1250°C). On the other hand,

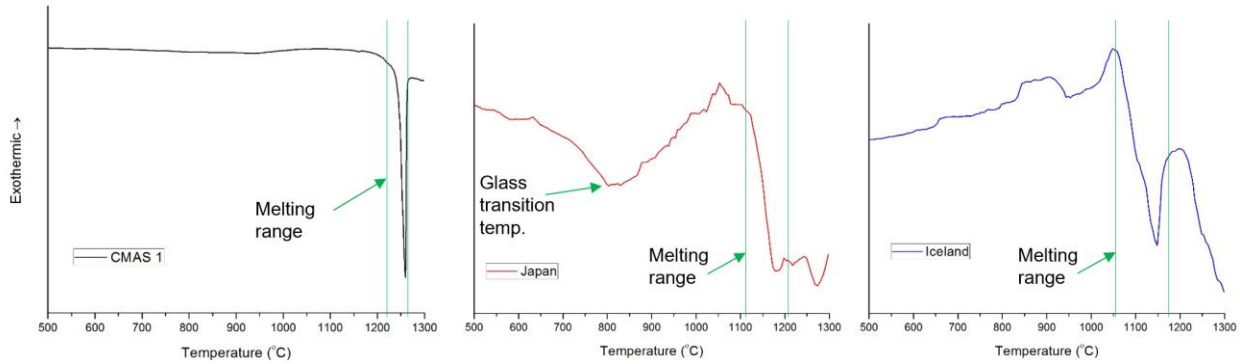


Figure 4.1: DSC profiles for CMAS 1 (black), Japan VA (red) and Iceland VA (blue).

the VAs exhibit lower melting point 1175°C and 1150°C for Japan and Iceland respectively and a broad melting range (>75°C).

4.2 XRD Results for CMAS/VA.

The XRD patterns for the used CMAS/VA powders as produced and collected are shown in the appendix section. The Iceland VA shows low intensity peaks indicating its amorphous nature. On the other hand, the Japanese VA shows a tendency for low content of crystal structures corresponding mostly to anorthite. CMAS 1 shows a crystalline nature with higher intensity peaks corresponding to pyroxene and anorthite.

4.3 Short Term Infiltration Tests in Standard 7YSZ Coatings

The short term infiltration behavior on the 425 μm thick EB-PVD 7YSZ coatings with CMAS 1 and VAs was studied by means of SEM and EDS analysis. **Figure 4.3a** shows the EDS elemental mapping of silicon trace (green) in all the samples after 0.5 min. infiltration. The figures show a significant infiltration in all the cases (>150 μm). **Figure 4.3b** shows the progression of infiltration over time for CMAS/VA after short term tests performed at 1250°C. The obtained results for infiltration progression over time show the maximum infiltration for the

Iceland VA (full coating infiltration after 2 min.), followed by CMAS 1 (395 μm after 5 min.) and Japan VA (295 μm after 5min.).

The infiltration results from **Figure 4.3b** show the most abrupt infiltration progression over time for CMAS 1 going for 155, 240 and 395 μm for 0.5, 2 and 5 min. respectively. The lowest progression is shown by the Japanese volcanic ash having a progression of 160, 210 and 295 μm for 0.5, 2 and 5 min. respectively. The infiltration progression for Iceland VA ranges in the middle going from 325 to 385 μm from 0.5 to 2 min. respectively. The data for 5 min. infiltration is not considered since the Iceland VA might have fully infiltrated the coating before 5 minutes. Comparing the first infiltration range from 0.5 to 2 minutes (90 sec.), CMAS 1 exhibits a more aggressive infiltration progression of 85 μm compared to 60 and 50 μm for Iceland and Japan. Additionally, the infiltration progression seems to have a linear growth by looking at the results plotted for CMAS 1 and Japan ash, whereas for Iceland ash one more reference point is required to determine the behavior of the infiltration curve.

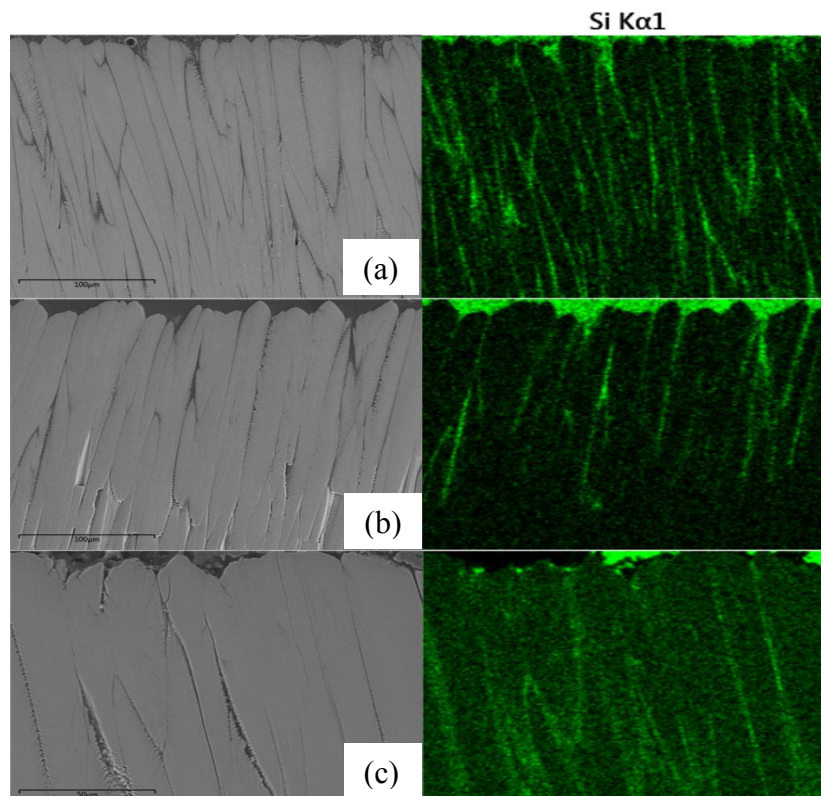


Figure 4.3a: Silicon elemental mapping for infiltration determination for Iceland (a), Japan (b) and CMAS1(c) for 0.5 min. infiltration at 1250°C.

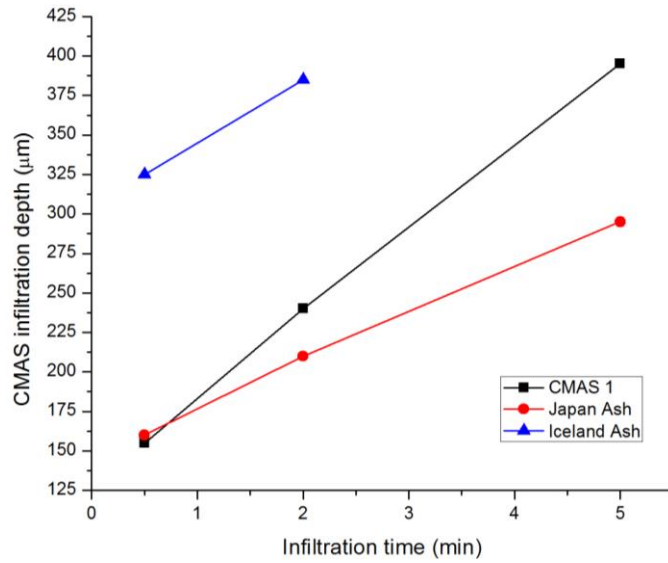


Figure 4.3b: Infiltration progression for CMAS/VA on 7YSZ samples at 1250°C for different times.

4.4 XRD Results for CMAS/VA-Yttria Mixtures

Figure 4.4 shows the obtained XRD patterns for all the CMAS/VA-yttria rich zirconia mixtures at 1250°C for 10 h. With the 65 wt.% yttria mixture three main phases are shared between the 3 CMAS/VA compositions: YSZ, oxyapatite and garnet, labeled in the patterns as #, + and & respectively. The shared phases are grouped on the top right side of the figure and the phases three phases grouped below are exhibited in individual CMAS reactions.

The first shared phase identified as garnet (&) exhibits the highest intensity for CMAS 1, followed by Iceland ash and Japan ash at the end. For all the CMAS compositions, the Garnet phase exhibited a peak overlap for two garnet types identified as Aluminum Iron Yttrium Oxide ($\text{Al}_4\text{FeY}_3\text{O}_{12}$) and Andradite ($\text{Ca}_3\text{Fe}_2(\text{Si}_3\text{O}_{12})$). However, for the volcanic ashes cases, the $\text{Al}_4\text{FeY}_3\text{O}_{12}$ exhibits a better peak matching and intensity. In the case of CMAS1, the garnet providing a better matching is Andradite. Elis et al. reported the formation of a garnet phase

exhibiting CMAS sealing properties using yttria rich coatings, the garnet was characterized with a good peak matching for the composition named “YAG” ($Y_3Al_5O_{12}$) [20].

The second common phase in the CMAS mixtures also exhibits a peak overlap. The identified phase corresponds to oxyapatite (+) with two matching candidates corresponding to Yttrium Oxide Silicate ($Y_{4.67}(SiO_4)_3O$) and Calcium Yttrium Oxide Silicate ($Ca_4Y_6(SiO_4)_6O$). For all the CMAS compositions, the ($Y_{4.67}(SiO_4)_3O$) shows the best peak matching and intensity. Additionally, the found oxyapatite phase has been reported in literature for yttria rich CMAS resistant coatings providing CMAS arrest properties [16, 38, 20, 21].

The last common identified phase corresponds to a phase of fluorite nature identified as Zirconium Yttrium Oxide or YSZ (#) with a chemical composition of ($Zr_{0.82}Y_{0.18}O_2$). This phase only exhibits a peak overlap with the Iceland ash mixture with the identified phase Yttrium Titanium Zirconium Oxide or YTZ ($Zr_{0.62}Y_{0.20}Ti_{0.18}O_{1.90}$). The YTZ phase exhibits higher intensity peaks with a similar matching. Additionally, one extra phase is identified only for the Iceland ash mixture exhibiting a mid-intensity and low-intensity peaks at about 31° and 36° respectively. The phase is identified as zirkelite (\$) with a composition of $CaZrTi_2O_7$, no additional information has been reported about this phase.

Finally, the Japan ash mixture exhibits an extra mid-intensity peak at about 27.5° corresponding to the common silicate mineral anorthite ($CaAl_2Si_2O_8$) bearing the common CMAS elements. The phase might be present from crystallization of unreacted CMAS glass.

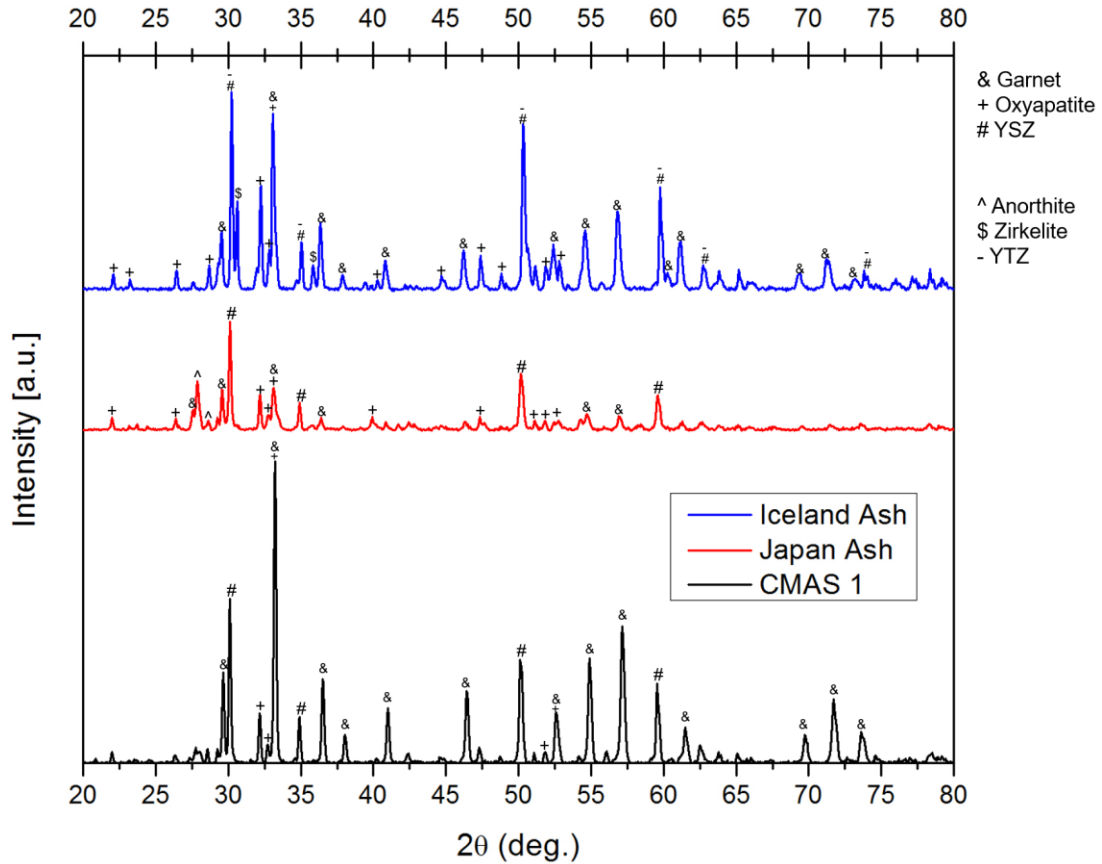


Figure 4.4: XRD patterns of CMAS/VA + 65% yttria rich zirconia-mixtures at 1250°C after 10 h.

4.5 CMAS Short Term infiltration Test on Yttria Rich Coatings.

Short term infiltration of 5 min. was used on the 65 wt. % yttria coatings at 1250°C to categorize the initial reaction products formed in order to obtain a better overview of which products contribute for CMAS initial crystallization. **Figure 4.5a** shows the overall cross-section views for the CMAS infiltrated samples. It can be seen from the image that the infiltration depth of the unreacted glass into the TBC is not uniform and more infiltration is seen where big columnar gaps (marked with arrows) are available in the coating structure. An estimation of infiltration is used by maintaining an overall infiltration area (delimited in the red bars) where no big gaps are available for deep glass infiltration. The infiltration is then estimated as 38, 28 and

28 microns for CMAS 1, Japan and Iceland VA respectively. The area marked within the yellow rectangle represents the reaction layer formed at the coating/glass interphase. Additionally, the **Figure 4.5b** shows a higher magnification of the reaction layer generated (yellow rectangle) where the columnar coating gaps are sealed by the formation of reaction products.

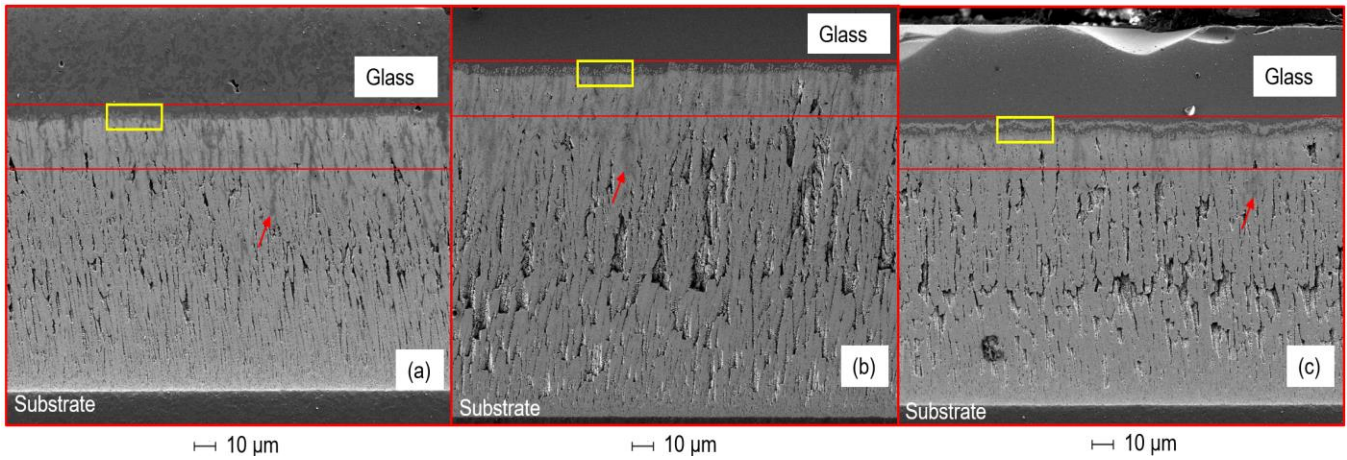


Figure 4.5a: Infiltrated zone image for (a) CMAS 1, (b) Japan VA and (c) Iceland VA after 5 min. infiltration at 1250°C.

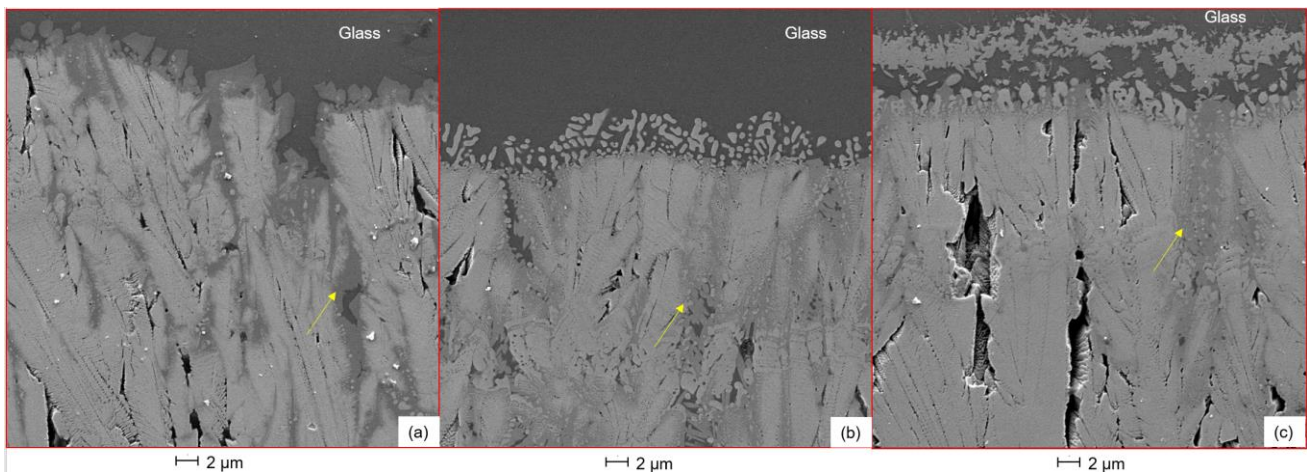


Figure 4.5b: High magnification image for the reaction layer at the coating/glass interphase for (a) CMAS 1, (b) Japan VA and (c) Iceland VA.

4.5.1 CMAS 1 Short Term Infiltration

Figure 4.5.1a shows the SEM cross section image of the reaction zone where the sealing of inter-columnar gaps by the bright gray product identified (by EDS and XRD results) as “Garnet” and labeled in the image as & can be observed. The dark gray uniform colored product at the top of the image and at the center of the columnar gaps represents the CMAS glass and it is labeled in the image as *. Another CMAS crystallizing product was found at the interface with the columnar gap and exhibits a brighter gray coloration than the garnet. The product was identified as oxyapatite and it was labeled as +. **Figure 4.5.1b** shows a higher magnification view of the area labeled with + and highlights where the oxyapatite product was found. The chemical composition of the products was analyzed by means of EDS spot analysis and characterized by comparing with the XRD results obtained at 1250°C isothermal heating for 10 hours. Finally, the **Table 4.5.1** provides a summary for the chemical composition of the found elements with their respective found phases.

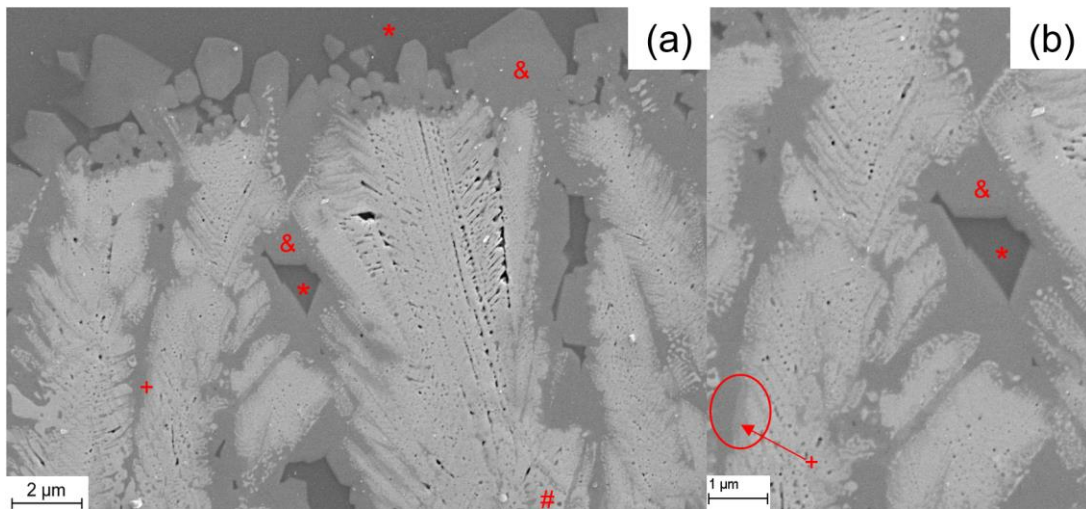


Figure 4.5.1: (a) CMAS1 reaction layer showing crystallization of the glass. (b) Higher magnification view for the label + product from figure (a).

Table: 4.5.1: Summary of reaction products for CMAS 1

Label	Chemical composition (Wt. %)								Phase
	O	Si	Ca	Mg	Al	Fe	Y	Zr	
&	35.81	9.4	9.5	3.3	4.5	11.1	19.8	5.7	Garnet
+	30.3	6.6	5.8	2.5	3.3	2.9	33.2	14.9	Oxyapatite
#	30.23	0.8	0.8	0.3	0.5	0.8	17.7	48.9	YSZ
*	45.2	18.4	13.9	4.8	8.5	4.0	2.3	2.2	CMAS Glass

4.5.2 Japan Ash Short Term Infiltration

Figure 4.5.2 shows the SEM cross sectional view of the initial crystallization process. The chemical composition of the labeled products in the image is shown in **Table 4.5.2** with their matched XRD phase obtained from the performed studies in the section 4.4. The enlarged prismatic crystals growing from side to side closing the columnar gap have been identified as the initial CMAS sealing products. The crystals are identified in the picture with a + sign and their chemical composition is matched for the Oxyapatite ($\text{Ca}_4\text{Y}_6(\text{SiO}_4)_6\text{O}$) phase which has been previously reported in literature [16, 20, 38, 21, 19] as a CMAS arresting product. It is clearly seen from the image the sealing performance of the oxyapatite product by sealing the columnar gaps present in the coating, at the right side it is observed how the smaller columnar gaps are sealed with this dark gray colored reaction product. The reaction product labeled as # with a bright white color and globular shape corresponds to a Zirconium Yttrium Oxide cubic phase (YSZ) with a lower Yttrium content than the present in the original yttria rich coating (65 wt. %). Finally, the dark product labeled * represents the glass. The chemical composition shown for the unreacted glass shows a high yttrium content confirming the reactivity of the coating with the molten glass.

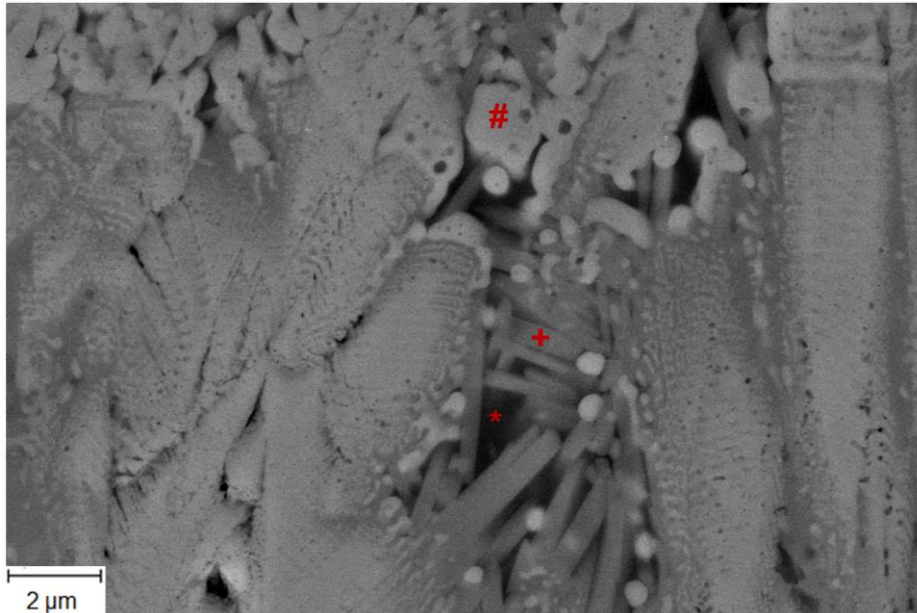


Figure 4.5.2: VA/yttria rich zirconia reaction zone showing the crystallization of the glass into a columnar gap sealing product.

Table 4.5.2: Composition of identified phases from Japan ash reaction zone.

Label	Chemical composition (Wt. %)								Phase
	O	Si	Ca	Mg	Al	Fe	Y	Zr	
+	31.4	13.1	4.6	1.0	0.9	0.0	49.0	0.0	Oxyapatite
#	27.9	4.7	1.2	0.6	1.2	1.5	22.7	40.2	YSZ
*	37.1	17.5	4.9	2.4	5.1	5.3	27.0	0.0	CMAS Glass

4.5.3 Iceland Ash Short Term Infiltration

Figure 4.4.3 shows the SEM section of the CMAS crystallization. The initial reaction has produced the both sealing products garnet and oxyapatite which were already seen in CMAS 1 and Japan ash respectively. The Garnet phase seems to be present where a large amount of reaction products are gathered together making an enlarged uniform crystal with a globular shape exhibiting a more contrasted dark gray coloration. The EDS spot analysis reveals all available

cations are present in the identified garnet phase (Ca,Mg,Si,Al,Fe,Y,Zr) with an enrichment in Fe.

The oxyapatite phase exhibits a similar elemental presence but with an enrichment in Zr possibly due to the proximity with the YSZ white globular crystal located below. The YSZ product shows a similar composition and white globular appearance exhibited in the other two used CMAS/VA sources and enrichment in Zr with Y depletion. The unreacted glass exhibits enrichment in Y and small traces lower than 0.8 wt. % of the original VA glass elements such as K and Na. **Table 4.4.3** provides a summary of the found phases with their respective measured chemical compositions.

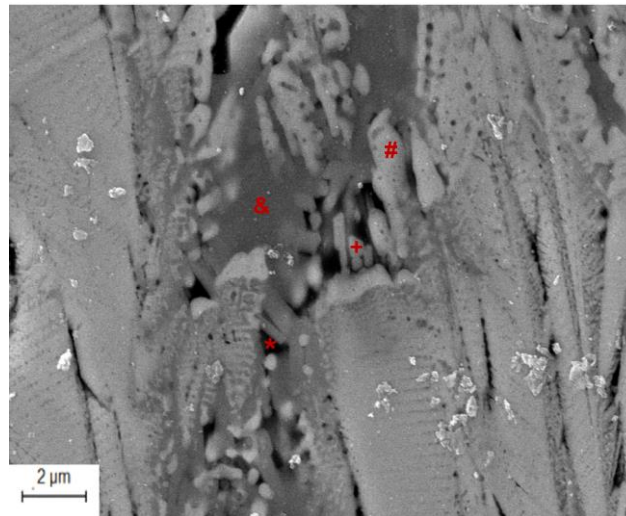


Figure 4.4.3: Reaction zone for Iceland ash showing the crystallization of the glass.

Table 4.4.3: Composition of reaction phases of Iceland ash reaction zone.

Label	Chemical composition (Wt. %)								Phase
	O	Si	Ca	Mg	Al	Fe	Y	Zr	
&	30.6	7.0	3.3	3.2	5.8	13.2	33.6	3.4	Garnet
+	29.9	9.3	3.4	0.6	1.3	0.0	38.7	16.6	Oxyapatite
#	26.31	2.5	1.0	0.6	1.3	1.8	28.9	37.7	YSZ
*	34.8	15.0	4.9	1.1	4.5	1.8	32.1	5.1	CMAS Glass

4.6 Long Term infiltration on Yttria Rich Coatings at 1250°C.

The long term isothermal infiltration tests were performed to study the coating infiltration resistance over increased periods of time (1 to 20 hours). In the case of long term infiltration, the coatings exhibited a deeper infiltration in larger cracks -columnar gaps compared to normal columnar gaps. **Figure 4.6a** shows the EDS elemental mapping (element Si) for the Iceland VA after 20 h. of thermal exposure which confirms infiltration depth as 60 μm . Using the same measurement technique CMAS 1 exhibits an infiltration of 65 μm and Japan ash 45 μm .

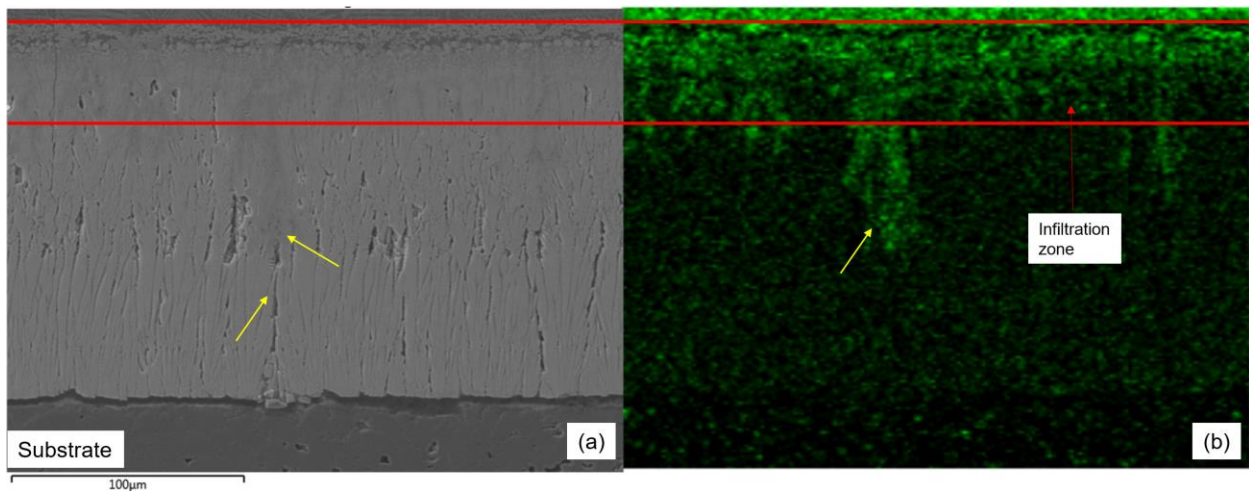


Figure 4.6a: Infiltration measurement for Iceland ash after 20 h. isothermal test at 1250°C. (a) SEM cross sectional view, (b) EDS elemental mapping for Si. Yellow arrows exhibit deep infiltration in large columnar gaps.

The infiltration progression over time is considered by comparing the progression of CMAS infiltration from the shortest infiltration test performed (5 minutes) with the longest one (20 hours) as shown in **Figure 4.6b**. By using this approach, the largest progression is shown by Iceland VA followed by CMAS 1 and Japan VA with a progression of 32, 27 and 20 μm respectively.

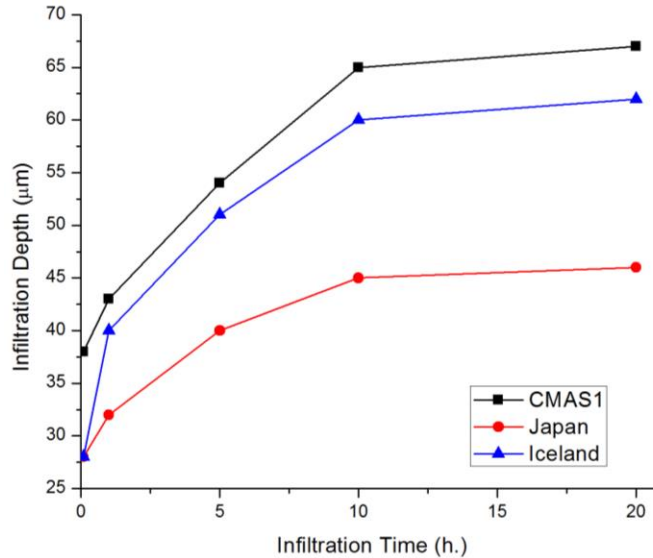


Figure 4.6b: Infiltration depth progression over time for thermal tests at 1250°C.

4.6.1 Reaction Layer Analysis for CMAS 1

The growth in the reaction layer formed at the CMAS glass/coating interface is explained in detail for each used CMAS/VA source in the following sections. The analysis of the reaction layer was performed by categorizing the formed reaction products by matching the product chemical composition with the found phase from the XRD results discussed in section 4.4. This analysis provides an insight for the time dependency on reaction products formation.

Figure 4.6.1a shows the reaction layer formed at the CMAS/TBC interface with the respective elemental mapping showing the main reaction elements for CMAS 1 infiltration after 1 hour of isothermal heating. It can be clearly seen from the elemental mapping how the garnet top layer (&) shows all the available cations from the CMAS/yttria sources (Y, Si, Al, Ca, Mg, and Fe). Another crystallized product with an appearance of enlarged dark prismatic shape is found on the top and it was identified as anorthite (^). The elemental mapping shows the enrichment of Al, Ca and Si in the crystallized product and the composition was confirmed by EDS elemental mapping. Additionally, the anorthite crystals do not seem to show CMAS arresting properties, since they are a crystal phase already present in the CMAS 1 powder. The

YSZ (#) phase is also found at the bottom of the reaction zone. The elemental mapping shows the Zr enrichment of the YSZ phase and the chemical composition obtained from EDS spot analysis confirms the Zr enrichment. The Y:Zr ratio of the YSZ phase was calculated to be 1:1.5 wt. % showing Y depletion compared to the ratio of the original coating (3.7:1 wt. %). The summary of the found phases and their elemental compositions are shown in **Table 4.6.1**.

The total reaction layer is considered from the formation of the garnet phase to the end of the YSZ phase (& and # respectively) in **Figure 4.6.1**. The total reaction layer exhibits a uniform thickness of 22 μm for 1 hour isothermal heating. Additionally, the garnet and YSZ phases showed a uniform thickness as well of 12 and 3.8 μm respectively. The oxyapatite layer is only traced in small localized areas such as feather arms where small amounts of CMAS glass are available for reaction.

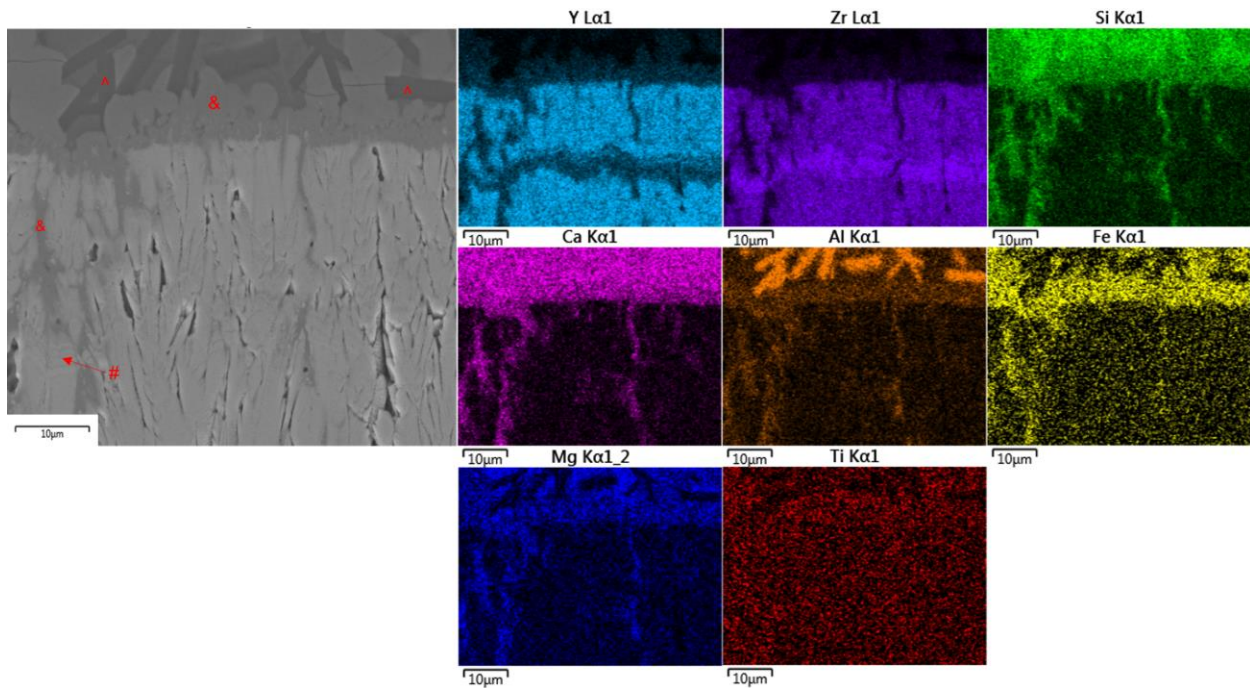


Figure 4.6.1a: Elemental mapping for CMAS 1 reaction zone after 1 h. 1250°C infiltration.

Table 4.6.1: Summary of reaction products for CMAS 1 1h. 1250°C infiltration.

Label	Chemical composition (Wt. %)								Phase
	O	Si	Ca	Mg	Al	Fe	Y	Zr	
&	31.0	11.9	12.7	3.7	5.0	15.0	19.1	0.0	Garnet
^	42.8	21.5	17.8	0.4	17.8	2.1	0.0	0.0	Anorthite
#	24.1	0.0	0.3	0.0	0.0	0.0	25.0	50.6	YSZ

Furthermore, The CMAS 1 reaction does not show significant changes regarding reaction appearance and formation of new crystalline phases. After 20 h. of isothermal heating, the garnet (&) phase is still present as the main CMAS crystallization product. Moreover, **Figure 4.6.1b** shows how the reaction layer changes with respect to time of infiltration for the thermal tests performed for 5 min., 5 h and 20h. From the figure it can be seen how the top garnet sealing phase increases its thickness with respect to time starting from 4 μm after 5 min. to 21 microns after 20 h.

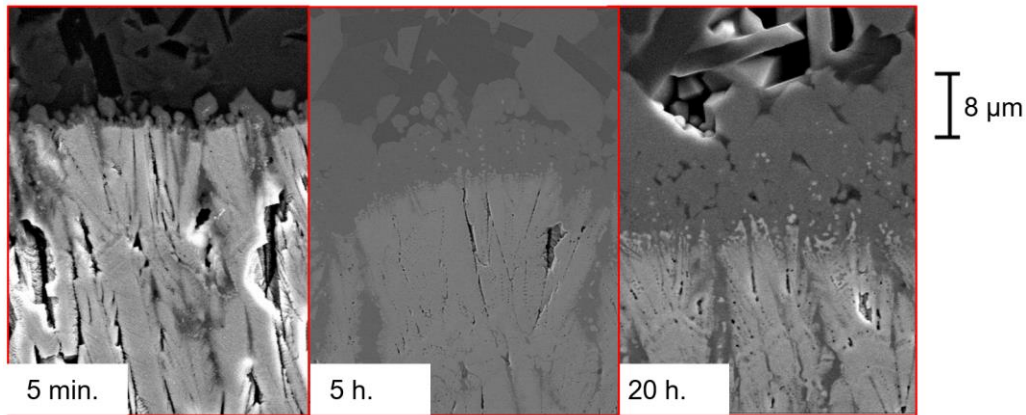


Figure 4.6.1b: Reaction zone progression for CMAS 1 at 1250°C.

4.6.2 Reaction Layer Analysis for Japan Ash

Figure 4.6.2a shows the top reaction layer formed for the Japan VA after 1 hour isothermal heating test at 1250°C. A large amount of enlarged mountain like shaped crystals are formed with a large thickness up to 17 μm . The elemental mapping and EDS chemical

composition for the enlarged mountain like particles show an enrichment of Silicon and Yttrium which provides a match for the oxyapatite Yttrium Silicate Oxide phase (+). It is also seen from the elemental mapping the formation of the fluorite YSZ (#) layer rich in Zr. There was a small localized trace of garnet (&) phase formation in the Japan VA reaction zone due to the large Si and low Fe compositions available in the ash the formation of Fe-Y rich garnets is not accelerated rather, the reaction is started with the large amounts of Si promoting the formation of the monolith type oxyapatite Y-Si rich crystals (+). **Table 4.6.2** provides a summary of the reaction product formed with their respective chemical composition.

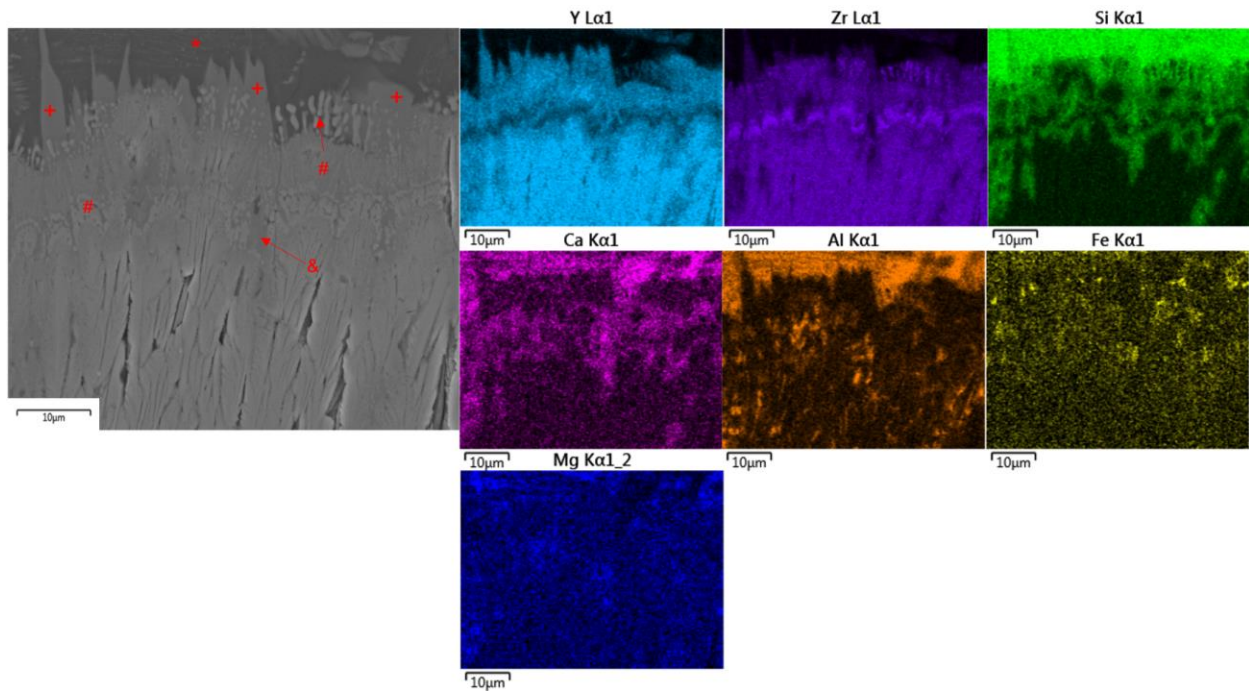


Figure 4.6.2a: Reaction layer for Japan VA with elemental mapping at 1250°C test after 1 h.

Table 4.6.2: Summary of reaction products for Japan VA 1250°C 1 h. isothermal.

Label	Chemical composition (Wt. %)									Phase
	O	Si	Ca	Ti	Mg	Al	Fe	Y	Zr	
&	30.5	5.4	2.6	0.0	1.9	8.6	10.7	35.4	5.0	Garnet
+	32.6	15.3	1.0	0.0	0.3	0.5	0.6	43.1	6.6	Oxyapatite
#	25.6	1.5	0.5	0.0	0.0	0.3	0.9	22.8	48.3	YSZ
*	40.8	24.2	5.0	0.0	1.7	9.5	5.5	6.6	3.2	Glass

After long time exposures, a significant growth in the formation of the oxyapatite crystals is exhibited followed by a reduction in the amount of globular YSZ bright particles laying on top of the coating. **Figure 4.6.2b** shows progression in the reaction layer after long term thermal exposure. It can be seen the oxyapatite crystals growth as large monoliths in localized areas with a columnar thickness up to 24 μm .

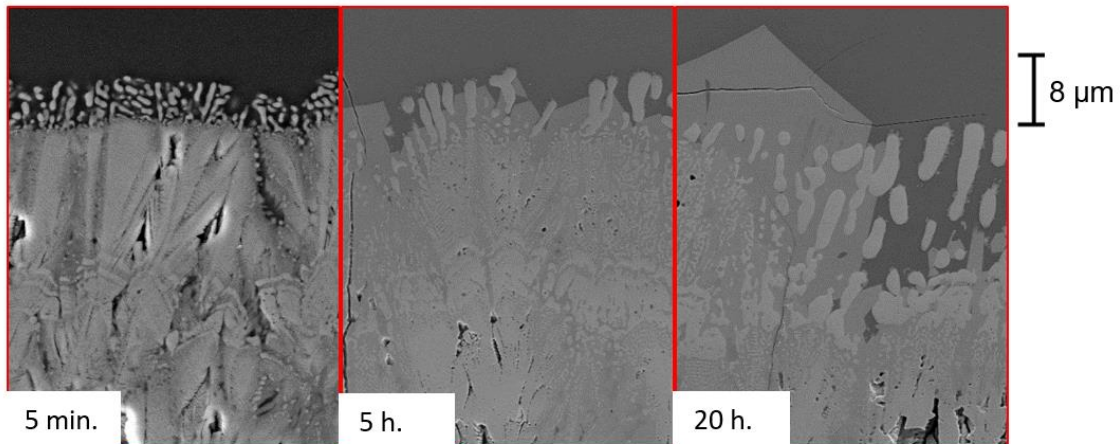


Figure 4.6.2b: Reaction layer progression for Japan VA at 1250°C.

4.6.3 Reaction Layer Analysis for Iceland Ash

Figure 4.6.3a shows the reaction layer formed at the VA/TBC interface with the respective elemental mapping showing the main reaction elements for Iceland ash infiltration after 1 hour of isothermal heating. A uniform layer in combination of garnet/oxyapatite with degraded TBC columns which corresponds to the area highlighted red in the **Figure 4.6.3a** is formed. Another layer of white bright prismatic particles is formed on the top of the reaction zone, this layer is identified from the EDS mapping as a Ti rich layer corresponding to the YTZ

(-). Also, large garnet crystals (&) are spotted exceeding the thickness of the top titanium rich layer. Finally, dendritic/diamond particles embedded in the unreacted glass on top are formed for all the long term isothermal tests. The dendritic particles labeled as “=” are identified as garnets as well due to the enrichment in Y-Fe and presence of other unreacted glass cations (Ca, Mg, Al, Si). **Table 4.6.3** provides a summary of the labeled reaction products with their XRD matched crystal phase.

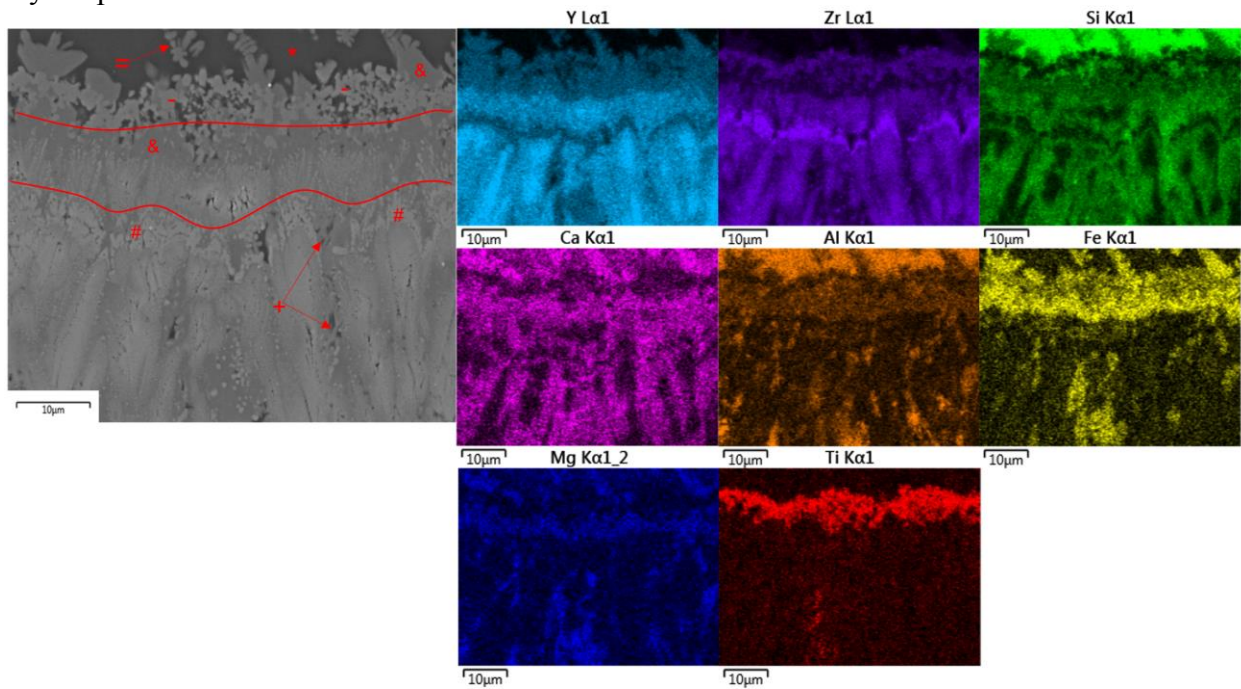


Figure 4.6.3a: Reaction layer for Iceland VA at 1250°C after 1 h. with elemental mapping.

Table 4.6.3: Summary of reaction products for Iceland VA.

Label	Chemical composition (Wt. %)									Phase
	O	Si	Ca	Ti	Mg	Al	Fe	Y	Zr	
&	29.0	7.5	5.0	0.9	2.9	3.0	21.9	23.72	0.0	Garnet
+	26.4	11.6	5.0	0.7	0.7	0.9	2.0	47.5	6.0	Oxyapatite
#	25.0	0.0	0.0	0.5	0.0	0.3	1.3	19.8	53.0	YSZ
=	33.3	11.8	6.7	1.0	3.5	3.3	17.8	21.8	0.0	Garnet/dendritic
-	27.8	0.8	1.1	11.7	0.4	1.0	12.2	21.5	23.7	YTZ
*	40.0	30.4	4.8	1.2	1.9	9.3	3.8	0.0	4.8	Glass

Figure 4.6.3b shows the progression in the reaction layer with respect to time. After 5 hours of isothermal heating, the garnet/oxyapatite mixture seems to have a recession in thickness and more small localized crystals are formed. It is also seen for this VA mixture that the small localized particles with a prismatic shape exhibit a chemical composition matching the oxyapatite phase (Ca-Y-Si rich), whereas the formation of the garnets is seen when large amount of glass is available to provide enough Fe in order to form the large globular garnet particles. For 10 h. infiltration (which is not shown here), the garnet phases seem to stabilize increasing its thickness to 18 μm while the Ti rich layer reduces in thickness of about 3 μm . Meanwhile, the YSZ layer appears to have a reduced growth in thickness of only a 4 μm after 10 hours of isothermal heating. After 20 h heating a reduction in TBC thickness is noticed of about 10 to 5 μm and a very large amount of dendritic particles are exhibited embedded in the unreacted glass which suggest that considerable amounts of Y that are leached out from the coating are diffusing slowly into the glass with respect to time generating this dendritic Y-Fe rich particles of garnet nature. Though the top embedded dendritic particles (\Rightarrow) identified as garnets, they do not seem to show sealing properties for the glass, instead, they seem to appear as reaction sub-products forming from the small amount of Y leached out form the coating.

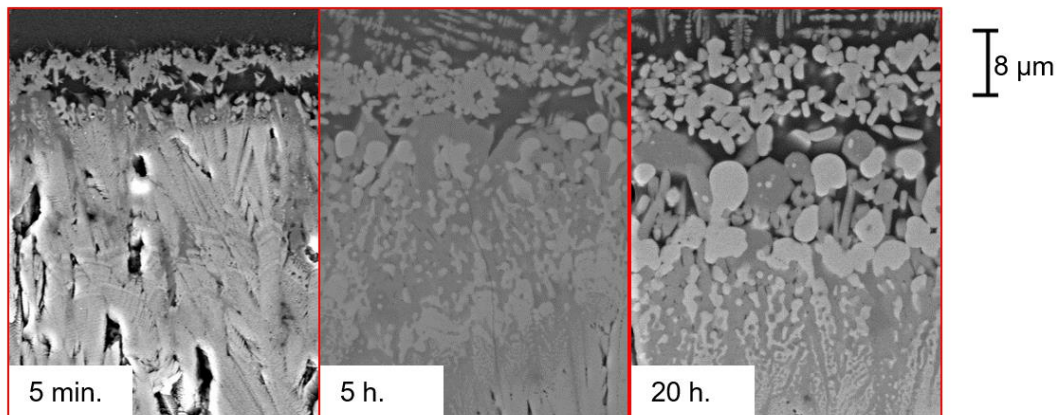


Figure 4.5.1b: Reaction zone progression for Iceland VA at 1250°C thermal tests.

4.7 Long Term Infiltration for 1225°C

Long term infiltration for CMAS/VA test were performed at 1225°C for a duration of 10 h. to identify a temperature influence in the reaction products formed. The studies were performed at the glass/TBC interface to identify if other reaction products are formed at lower temperatures. For comparison purposes, the temperature was selected for the starting melting point available for CMAS 1 (1225°C) source as exhibited from the DSC results in order to ensure that some molten glass would be available for reaction to take place.

4.7.1 Reaction Layer Analysis for CMAS 1

Figure 4.7.1 shows a comparison of the reaction layers formed at 1225 (a) and 1250°C (b) after 10 h. isothermal heating exposure. At 1225°C the formation of the garnet phase (&) is still present as the main CMAS sealing product available. The garnet layer can be seen at the top of the TBC columns with a dark gray contrast as seen as well for 1250°C infiltration test. The main difference in the garnet products is their layer thickness of 6 and 17 μm for 1225 and 1250°C respectively. Additionally, the formation of the anorthite crystals (^) and YSZ (#) layers are also seen both reaction layers. **Table 4.7.1** shows the summary of the reaction products found in the interface layers for both infiltration tests. The reaction products do not exhibit a large difference in their chemical composition which emphasizes the minimal temperature dependence in the reaction product formation.

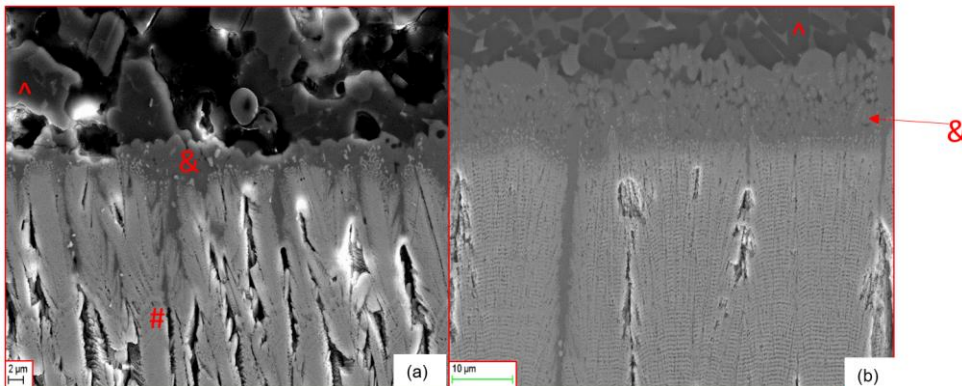


Figure 4.7.1: Reaction layer formation for CMAS 1 after 10 h. thermal exposure at (a) 1225°C and (b) 1250°C.

Table 4.7.1: Reaction products summary for CMAS 1 after 10 h. thermal exposure.

Temp. (°C)	Label	Chemical composition (Wt. %)									Phase
		O	Si	Ca	Ti	Mg	Al	Fe	Y	Zr	
1225	&	34.5	11.9	11.2	1.4	4.5	4.3	11.8	20.3	0.0	Garnet
1250	&	32.6	15.3	1.0	0.0	0.3	0.5	0.6	43.1	6.6	Garnet
1225	^	45.5	20.4	13.8	0.0	0.3	17.9	2.0	0.0	0.0	Anorthite
1250	^	44.9	20.4	13.7	0.1	0.8	16.1	1.8	0.6	1.6	Anorthite
1225	#	24.7	0.0	0.5	0.0	0.0	0.0	0.0	22.4	52.5	YSZ
1250	#	22.8	0.0	0.0	0.0	0.0	0.0	0.0	16.5	60.7	YSZ

4.7.2 Reaction Layer Analysis for Japan Ash

The reaction layer for the Japan VA seems the same for 1225 and 1250°C as seen in **Figure 4.7.2**. The oxyapatite phase is highly predominant as the glass crystallization product for molten glass. The YSZ (#) layer is also formed uniformly for both samples on top and bottom of the reaction layer zone. The summary of the chemical composition for the reaction products is shown in **Table 4.7.2**. The products do not exhibit as well a significant change in their chemical composition which suggest no temperature dependency on the formation of reaction products for the Japan VA reaction.

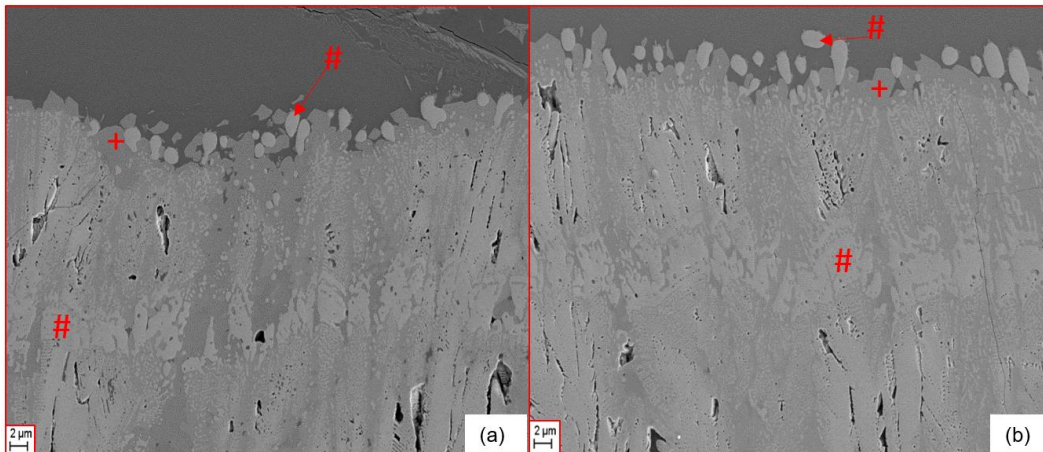


Figure 4.7.2: Reaction layer for Japan VA after 10 h. infiltration at (a) 1225 and (b) 1250°C.

Table 4.7.2: Summary of reaction products for Japan VA.

Temp. (°C)	Label	Chemical composition (Wt. %)									Phase
		O	Si	Ca	Ti	Mg	Al	Fe	Y	Zr	
1225	+	30.0	11.9	4.7	0.0	0.6	0.8	0.8	43.1	3.1	Oxyapatite
1250	+	31.7	11.2	3.9	0.0	0.6	1.2	0.0	45.7	5.8	Oxyapatite
1225	#	25.6	0.0	0.0	0.0	0.0	0.0	1.2	16.1	51.9	YSZ
1250	#	23.6	0.0	0.3	0.0	0.0	0.0	0.9	20.0	55.2	YSZ

4.7.3 Reaction Layer Analysis for Iceland Ash

The reaction layer formed for the Iceland VA exhibits a similar appearance for 1225 (a) and 1250°C (b) after 10 h. of thermal exposure as shown in **Figure 4.7.3**. The reaction layer exhibits the same reaction products available for both thermal tests. The reaction layers generating glass crystallization still appear to be garnet (&) and oxyapatite (+). The main difference is shown for 1225°C which appears to have a higher presence in garnet particles throughout the top area between the YSZ (#) and YTZ (-). Additionally, the brighter oxyapatite particles (+) exhibit a more prismatic small appearance for 1250°C and a larger presence of degraded TBC columns are shown below the garnet area in between the YSZ (#) and YTZ (-) layers for 1250°C.

Table 4.7.3 shows a summary of the chemical composition for the reaction products found for each temperature. The reaction products do not exhibit a significant change in chemical composition after being exposed to two different temperatures. Only the top reaction products embedded in molten glass were found to have a difference in Y enrichment. The products have been identified before with a composition matching the garnet phase (&) having all cations available in the glass with an enrichment in Fe and Y. The phases have been referred as garnet/dendritic which seem to be sub-products from the reaction generated from the diffusion of Y into the glass. Their enrichment in Y at higher temperatures (1250°C) indicate a temperature dependency for the Y diffusion into the glass reservoir.

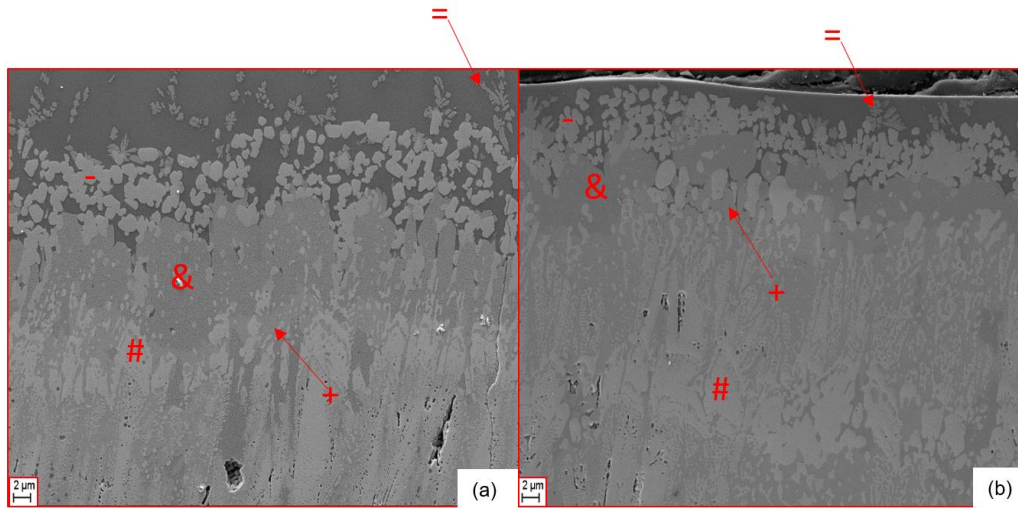


Figure 4.7.3: Reaction layer for Iceland VA after 10 h. infiltration at (a) 1225°C and (b) 1250°C.

Table 4.7.3: Summary of reaction products for Iceland VA.

Temp. (°C)	Label	Chemical composition (Wt. %)									Phase
		O	Si	Ca	Ti	Mg	Al	Fe	Y	Zr	
1225	&	30.3	8.7	5.6	0.6	3.0	2.5	17.2	32.1	0.0	Garnet
1250	&	31.3	8.7	5.5	0.7	3.4	3.4	16.6	29.3	0.0	Garnet
1225	+	28.9	9.4	4.4	0.0	0.4	0.0	1.2	45.2	10.4	Oxyapatite
1250	+	30.3	11.5	4.8	0.0	0.0	0.7	0.0	47.8	5.0	Oxyapatite
1225	#	25.2	0.4	0.0	0.0	0.3	0.3	1.6	18.0	54.3	YSZ
1250	#	24.3	0.0	0.0	0.0	0.0	0.0	0.9	17.7	56.6	YSZ
1225	-	28.7	1.8	1.0	12.0	0.3	1.4	10.8	21.3	22.3	YTZ
1250	-	27.2	0.0	0.5	11.0	0.2	1.1	11.6	21.6	26.6	YTZ
1225	=	37.3	16.3	2.5	1.6	3.6	5.1	19.6	8.4	3.1	Garnet/dendritic
1250	=	34.0	12.3	4.6	0.6	3.6	4.7	14.9	24.5	0.0	Garnet/dendritic

4.8 Infiltration Kinetics Analysis.

This section explains the CMAS infiltration kinetics -assuming low presence of chemical reaction slowing the molten glass flow into the columnar gap medium present in EB-PVD 7YSZ. The experimental results obtained from short term CMAS infiltration tests into standard 7YSZ coatings are used to provide baseline calculations and fitting parameters such as tortuosity for the

concentric pipe model introduced in section 2.5. The mathematical infiltration model proposed by Naraparaju et al. suggests that the TBC microstructure has a great influence on the infiltration behavior of the molten glass. In principle, CMAS infiltration resistance of a TBC can be increased by refining its microstructure splitting the path that the molten fluid has to travel by means of adding extra channels (“feather arms”). This splitting effect influences the tortuosity parameter (τ). The other parameters influencing infiltration are fluid properties such as viscosity and surface tension which are not influenced by the TBC microstructure rather the chemical composition and temperature of the melt.

4.8.1 Molten Fluid Properties Determination

The viscosity of the molten fluid was determined by using the model proposed by Giordano et al. [42] which uses the chemical composition of the major oxides present in the mineral sources. The model predicted viscosities of CMAS/VA are shown in **Figure 4.8.1**. A considerable difference between the volcanic ashes and CMAS 1 can be observed. Lowest viscosity is predicted for CMAS 1 ranging in the negative logarithmic values was predicted. The presence of alkaline oxides such as NaO and K₂O influences the higher viscosity predicted for Vas. Additionally, the large SiO₂ content has a major influence in increasing the viscosity of the fluid predicting the largest value for Japan VA which exhibits the largest silica content in its composition. However, experimental results in process for publication for CMAS viscosities show a large discrepancy in the model predicted values from the experimentally calculated values. The surface tension parameters were calculated by using equation 4 where only relevant oxides are considered in the chemical composition and the values are fixed at 1400°C. The calculated values were: **0.438, 0.364 and 0.396 N/m** for CMAS 1, Japan VA and Iceland VA respectively. The surface tension values do not exhibit a large difference, giving the highest for CMAS 1 and lowest for Japan VA.

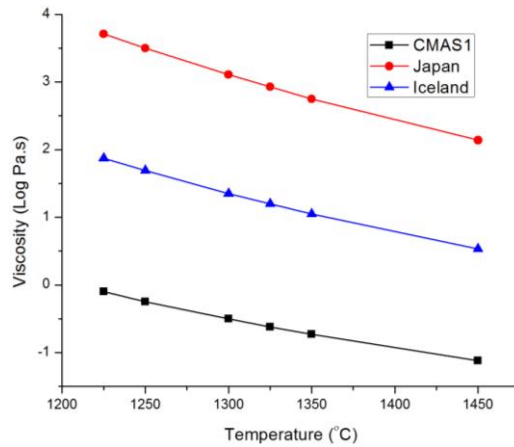


Figure 4.8.1: Calculated viscosity for CMAS/VA.

4.8.2 Permeability Analysis.

The TBC permeability was calculated for the single pipe and concentric pipe model to compare its approximation with the experimental results. **Figure 4.8.2** shows the variation on the permeability with respect to the used model. The plotted permeability (k) for the concentric pipe model (equation 4) is based on the common TBC microstructure parameters obtained from the as deposited 7YSZ samples where the radius of TBC column (kernel) is $8.5 \mu\text{m}$ and the columnar gap is varied from 1 to $4 \mu\text{m}$. Thus, the effective radius plotted for the concentric pipe model represents the kernel plus the columnar gap. The plotted radius for the open pipe model is based on the radius of the surface area available for infiltration matching the microstructural parameters of the concentric pipe (constant kernel size of $8.5 \mu\text{m}$ and columnar gap varying from 1 to $4 \mu\text{m}$) which was calculated to be $6.16 \mu\text{m}$ (equation 3). For comparison purposes the open pipe radius covered an area of 5.5 to $8.5 \mu\text{m}$. The tortuosity factor was kept fix at a value of 1.25 and pore fraction of 0.22.

The permeability curves show a significant difference in the values for the same infiltration conditions for each model. The results predict a higher permeability for the open pipe model widely used in literature. The significance of higher permeability is the prediction of a faster infiltration into the TBC by a factor of 6 for the same microstructural conditions which represents a large discrepancy compared with the concentric pipe model. In order to determine the accuracy of the models the calculation of infiltration time was compared with the experimental values obtained from short term infiltration on 7YSZ coatings.

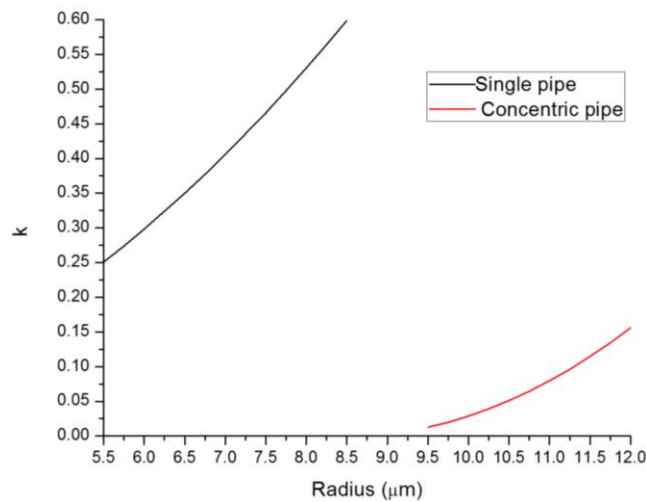


Figure 4.8.2: Permeability of single pipe vs. concentric pipe model.

4.8.3 Infiltration Prediction

The calculated infiltration was predicted for CMAS 1 since it exhibits the narrowest melting range of about 25 degrees with a fully molten state upon reaching 1250°C. The parameters for TBC microstructure were calculated as 0.22 pore fraction, permeability of 0.047 and a fitted tortuosity of 1.25. The contact angle was determined by measurements performed from a DLR research partner fixed at 1250°C giving an angle of 45°. Two viscosity values were used, the predicted from the Giordano model and the experimental viscosity obtained from the contact angle studies specified previously. The results shown in **Table 4.3.8** represent the

comparison in infiltration time for 395 μm depth in 7YSZ coatings using the predicted viscosity (Giordano model) and the experimental viscosity for CMAS 1. The results also compare the infiltration time obtained from the open pipe and concentric pipe models. The predicted results exhibit a significant disagreement in the infiltration time due to the large discrepancy in the viscosities (experimental and Giordano). For comparison purposes, the experimentally found infiltration depth of CMAS 1 after 5 min. (300 sec.) of thermal exposure at 1250°C was 395 μm as shown in the section 4.2. The results obtained for the concentric pipe model and the experimental measured viscosity show a good agreement with the infiltration time by showing a difference of 18 sec. compared to the experimental results of infiltration. Additionally, the predicted results for infiltration show a significant difference in the estimated time of infiltration between the open pipe model and the concentric pipe model. In order to reach a similar agreement in infiltration time between the open pipe model with the experimental infiltration results, a tortuosity factor needs to be set for a value of 8 which represents a very unrealistic value for a case of EB-PVD TBCs. Finally, the results clearly show a more realistic approach for infiltration prediction from the proposed concentric pipe model using the experimentally measured viscosity.

Table 4.8.3: Calculated times of infiltration for CMAS 1 at 1250°C.

	Viscosity (Pa.s)	Infiltration time (sec.)	
		Concentric	Open
Experimental viscosity	6.35	282.4	43.9
Giordano model viscosity	0.56	24.9	3.9

Chapter 5: Discussion

5.1 Infiltration Depth Analysis for High Yttria Coatings.

Figure 4.6b shows the infiltration depth progression for CMAS/VA with respect to time at 1250°C. The first feature to check about this plot is the minimal progression in the infiltration depth that yttria rich coatings exhibit with respect to time, showing the highest progression for Iceland VA of about 32 μm in a time span from 5 min. to 20 h. Besides, the graph shows a stabilization in the infiltration depth exhibiting a more linear behavior after 10 h. of thermal exposure which suggests that the reaction products remain stable sealing the gaps for further CMAS glass infiltration.

The maximum infiltration is exhibited by CMAS 1 with an infiltration depth ranging up to 65 μm . By only considering the effects of infiltration based on viscosities, the results are in good agreement by showing the highest infiltration for the lowest viscous fluid in this case CMAS 1. However, the kinetics of infiltration are also governed by the microstructure of the TBC and reactivity of the reaction products inducing glass crystallization.

It is also believed that the infiltrated glass in the large columnar gaps/cracks upon melting of the CMAS/VA freezes rather than progressing with respect to time. The conclusion is drawn by doing EDS spot analysis on the reaction products that are formed in large columnar gaps. **Table 5.1** shows the chemical composition of the reaction products for the tests performed for 5 min. and 20 h. at 1250°C. The chemical composition of the reaction products does not exhibit a substantial change with respect to time and mostly oxyapatite is found. Only an enrichment in Zr was found in the composition of the reaction products. This is due to the higher availability of Zr at small columnar gaps/cracks from where the 20 h. measurements were obtained. The conclusion is drawn as follows:

- 1) The induced crystallization of the melt does not take place fast enough to seal the large columnar gaps available in the coating allowing some glass to infiltrate deeper.

- 2) As the glass flows down into the TBC drop in Fe content in the melt makes the main reaction product to be oxyapatite.

Table 5.1: Summary of reaction products at infiltrated columnar gaps for 1250°C.

Time	Label	Chemical composition (Wt. %)									Phase
		O	Si	Ca	Ti	Mg	Al	Fe	Y	Zr	
5 min.	CMAS 1	29.8	8.0	5.2	0.4	3.3	4.8	3.1	28.2	8.3	Oxyapatite
20 h.	CMAS 1	30.8	7.1	6.2	0.8	3.4	3.2	3.9	25.7	18.9	Oxyapatite
5 min.	Japan VA	57.5	10.3	1.6	0.0	0.9	5.0	0.0	20.6	4.1	Oxyapatite
20 h.	Japan VA	25.8	6.7	2.6	0.0	0.6	0.4	0.0	37.8	25.8	Oxyapatite
5 min.	Iceland VA	28.1	7.8	2.0	0.0	0.6	1.3	0.0	53.6	6.4	Oxyapatite
20 h.	Iceland VA	27.8	6.9	2.4	0.0	0.4	1.4	1.3	48.7	11.2	Oxyapatite

5.2 Reaction Layer Growth of Yttria Rich Coatings.

The usual CMAS attack in EB-PVD 7YSZ system can be divided into the initial infiltration of the molten glass into the columnar gaps and porous features influenced by capillary forces and simultaneous dissolution of t'-YSZ grains into the glass and re-precipitation as new Zr rich destabilized phases depending on the chemistry of the glass. As in the case of 7YSZ, the dissolved materials in the glass do not generate a significant influence to crystallize the melt preventing further infiltration. If a CMAS resistant coating has to be developed, the criteria must be chosen in such way that the crystallization of the melt must act relatively faster than the capillary action sealing the columnar gaps before significant infiltration occurs preventing further infiltration. Additionally, after sealing of the gaps, the formed reaction products should be stable enough to saturate the glass reaction generating a uniform reaction zone with no significant growth over time.

In the case of yttria rich YSZ coatings, upon CMAS glass infiltration, the dissolution of Y into the glass quickly generates a re-precipitation of stable phases that seal the columnar gaps preventing further infiltration. The formed sealing phases in this interphase are oxyapatite (+) and garnet (&) and other available phases depending on the chemical composition of the melt. A detailed analysis of reaction layer and precipitation of glass sealing products will be discussed in the following sections for each CMAS/VA source.

5.2.1 Reaction Layer Analysis for CMAS 1.

Figure 5.2.1 shows a schematic of the formed reaction products at the TBC/molten glass interface. The first reaction product which grows is the oxyapatite (+) which crystallizes the glass in reduced areas such as feather arms and minor cracks/gaps where no significant amounts of Fe are available. Reaction progresses further, as more glass is available, with the formation of uniform Fe rich top garnet (&) phase. For CMAS 1, the garnet is the most stable phase present in the reaction layer that grows with respect to time starting from initial thickness of 4 μm (5 min.) and grows to 21 μm after 20 h. The constant growth of the garnet phase is believed to be due to the high presence of Ca and Fe in the glass which upon reaction with Y trigger the formation of garnet phase with enrichment in Fe and Y. As garnet forms, the extra Ca reacts with Al and Si forming a stable anorthite phase (^) present on top of the reaction as dark prismatic particles.

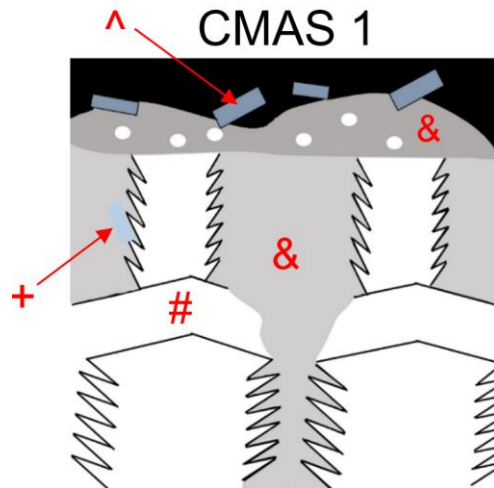


Figure 5.2.1: Reaction layer schematic for CMAS 1 at 1250°C.

The anorthite phase represents a stable phase which is reported to generate sealing properties for mitigation strategies using $\text{Al}_2\text{O}_3+\text{TiO}_2$ doping in 7YSZ coatings [36]. However, in this reaction the anorthite phase is only found on top of the reaction layer as a sub-reaction product without sealing capability. Since a large reservoir of glass is available, as anorthite is

formed the extra Fe keeps on acting as a source for Y generating a continuous growth of the garnet phase.

The YSZ fluorite layer (#) is formed as a byproduct due to the depletion of Y from the TBC inducing the glass crystallization. This phase does not seal the available gaps instead; it appears to form as a sub-reaction product triggered after the formation of garnet. **Table 5.2.1** provides a summary of the chemical composition of the reaction products that are formed after 5 min. and 20 h. at 1250°C in order to compare the changes in chemical composition with respect to time. It is clear from the chemical analysis that the composition of the reaction products does not have a significant variation with respect to time which suggest that the reaction is stable after long thermal exposure. Only the YSZ layer (#) exhibits a reduction in Y after 20 h. which is expected due to the continuous formation of Y-Fe rich garnet phase (&).

Table 5.2.1: Summary of reaction products for CMAS 1 at 1250°C.

Time	Label	Chemical composition (Wt. %)									Phase
		O	Si	Ca	Ti	Mg	Al	Fe	Y	Zr	
5 min.	&	29.4	9.7	9.8	1.2	3.0	4.4	12.2	15.7	0.0	Garnet
20 h.	&	34.2	10.8	10.9	1.4	3.8	5.5	13.4	19.9	0.0	Garnet
5 min.	^	40.2	18.1	12.9	0.0	0.6	15.1	2.1	0.0	0.0	Anorthite
20 h.	^	45.2	20.9	14.2	0.0	0.9	16.0	2.6	0.0	0.0	Anorthite
5 min.	#	27.1	0.0	0.4	0.0	0.0	0.0	0.0	25.0	50.6	YSZ
20 h.	#	22.8	0.0	0.0	0.0	0.0	0.0	0.0	16.5	60.7	YSZ

5.2.2 Reaction Layer Analysis for Japan VA.

Figure 5.2.2 shows the schematic representation of the reaction layer interphase between TBC/molten glass at 1250°C. Due to the low contents of Fe in the Japan VA, the main reaction product formed in the reaction layer is oxyapatite (+). In fact, the Fe-Y rich garnet phase was only traced for the Japan VA in small amounts at times <1 h. At longer time infiltration (>5 h.) the garnet phase was no longer traceable making the oxyapatite the predominant glass reaction

product. Due to this fact, the garnet layer is neglected as sealing product for Japan VA and only oxyapatite is considered. Since the chemical composition of the Japan VA is highly rich in Si, the reaction is driven by the leeching of Y from the coating generating the oxyapatite layer (+) and leaving two sub-reactions of YSZ (#) enriched in Zr on top and bottom of the reaction zone. The large reservoir of glass deposited generates a continuous diffusion of Y into the glass promoting the formation of large oxyapatite monoliths after long term exposures.

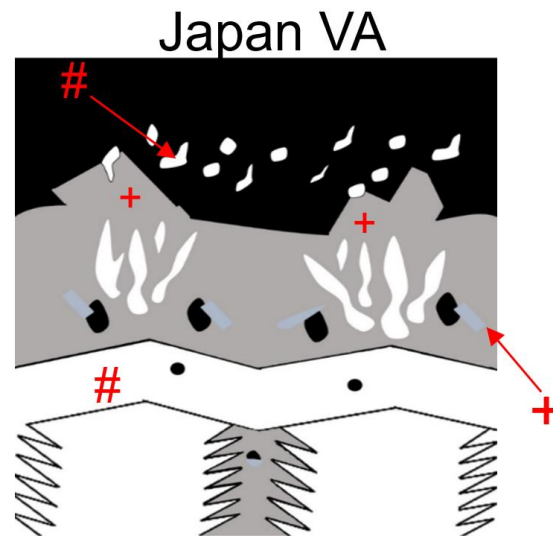


Figure 5.2.2: Reaction layer schematic for Japan VA at 1250°C.

Table 5.2.2 shows the summary of chemical composition of the formed reaction products after 5 min. and 20 h. of thermal exposure. The oxyapatite layer exhibits enrichment in Si and depletion in Ca after long term thermal exposure due to the accumulation of products in large monoliths which match the found XRD phase Yttrium Oxide Silicate ($Y_{4.67}(SiO_4)_3O$). The oxyapatite product present in the columnar gaps and in small prismatic particles exhibits the same composition as for the 5 min. product with a Ca content up to 5 wt. %. The change in the composition of the YSZ (#) layer with an increase of Zr follows the same trend for all reactions (CMAS/VA) due to the leeching of Y from original coating.

Table 5.2.2: Summary of reaction products for Japan VA at 1250°C.

Time	Label	Chemical composition (Wt. %)									Phase
		O	Si	Ca	Ti	Mg	Al	Fe	Y	Zr	
5 min.	+	28.7	9.2	3.9	0.0	0.4	0.4	0.0	48.0	9.2	Oxyapatite
20 h.	+	32.3	15.2	0.6	0.0	0.4	0.2	1.0	46.0	5.3	Oxyapatite
5 min.	#	28.8	5.1	1.5	0.0	0.8	1.7	2.2	15.7	43.7	YSZ
20 h.	#	25.0	0.0	0.0	0.0	0.0	0.0	1.7	18.5	54.0	YSZ

5.2.3 Reaction Layer Analysis for Iceland VA.

Figure 5.2.3 shows the scenario of reaction products formation of TBC/molten glass interphase of Iceland VA at 1250°C schematically. In this case the reaction is also started by the formation of the small prismatic oxyapatite crystals (+) generating the initial sealing of the molten glass. As more glass is available for infiltration, the localized oxyapatite crystals accumulate more Fe rich glass which precludes the formation of the larger garnet (&) crystals. As time progresses, the large molten glass reservoir deposited on top acts as a Y sink which induces the formation of the top dendritic garnets (=) rich in Fe-Y. As expected with respect to time exposure, the accumulation of dendritic particles embedded in the molten glass increases due to the constant diffusion of Y. This generates a reduction of the garnet particles available on the reaction layer as seen in **Figure 4.7.3** after 20 h. of thermal exposure. The depletion in Fe due to the accumulation on the dendrites (=) facilitates the formation of oxyapatite particles taking over the reaction as main crystallization products at the interface after longer thermal exposure (20 h.).

The available Ti in the chemical composition of the Iceland VA generates the formation of the sub-reaction product YTZ (-) localized on top of the reaction interphase as bright globular particles. The mentioned particles are not believed to have a significance in the crystallization of the glass. However, due to their enrichment in Y, they might be serving the reaction as Y source for the formation of the dendritic top garnets embedded in the glass.

The YSZ layer (#) formed at the bottom is generated also due to the depletion of Y in the original coating to generate the crystallization products. The layer exhibits an enrichment in Zr the same as seen for the CMAS 1 reaction.

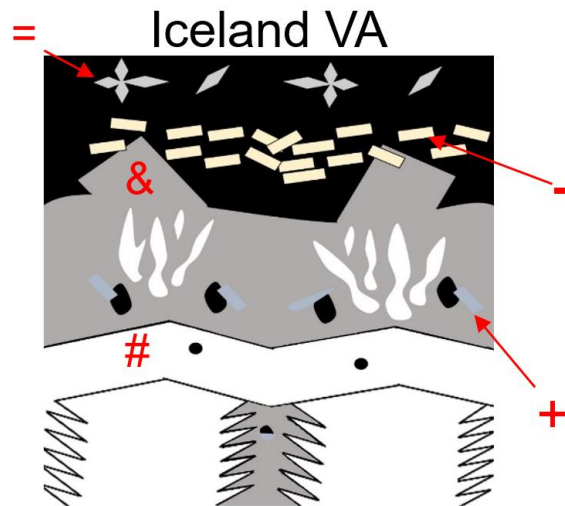


Figure 5.2.3: Reaction layer schematic for Iceland VA at 1250°C.

Table 5.2.3 shows the summary of the chemical composition for the reaction products after 5 min. and 20 h. for 1250°C. The table exhibits a minimal change in the chemical composition with respect to time for the reaction products identified in the reaction layer interphase. In general, the garnet/dendritic (=) reaction product exhibits the most noticeable change in its chemical composition compared to the other products. It exhibits an increase in Y with respect to time which confirms that the deposited glass acts as a sink for Y stabilizing new phases on top. The formation of the garnet phase induces a large depletion of Fe and Y in the coating which promotes a larger formation of oxyapatite particles which are more noticeable after longer term infiltrations (>10 h.).

Table 5.2.3: Summary of reaction products for Iceland VA.

Time	Label	Chemical composition (Wt. %)									Phase
		O	Si	Ca	Ti	Mg	Al	Fe	Y	Zr	
5 min.	&	30.6	7.0	3.3	0.0	3.2	5.8	13.2	33.6	3.4	Garnet
20 h.	&	30.1	7.5	4.8	0.6	3.1	3.8	19.5	30.7	0.0	Garnet
5 min.	+	30.2	9.6	4.1	0.0	0.8	1.9	1.6	38.4	13.0	Oxyapatite
20 h.	+	28.7	8.4	3.5	0.0	0.0	0.0	0.8	40.2	17.9	Oxyapatite
5 min.	#	32.1	0.0	0.0	0.0	0.0	0.0	0.0	13.4	54.6	YSZ
20 h.	#	25.1	0.0	0.0	1.5	0.0	0.0	2.3	18.8	52.4	YSZ
5 min.	=	41.6	14.8	3.0	1.8	2.4	4.3	18.0	8.7	3.5	Garnet/dendritic
20 h.	=	36.9	16.2	5.5	1.0	3.4	5.1	13.5	16.8	0.0	Garnet/dendritic
5 min.	-	27.7	1.2	0.7	9.8	0.5	0.9	11.0	21.0	27.3	YTZ
20 h.	-	28.8	1.8	0.6	10.4	0.3	1.5	11.6	19.6	25.7	YTZ

5.3 Temperature Dependency Analysis.

The only composition which appears to exhibit temperature dependency in the formation of reaction products is the Iceland VA. The temperature dependency appears to be present in the formation of the top garnet/dendritic products (=) at 1250°C which promotes a greater dissolution of Y into the molten glass, generating a reduction of garnets (&) in the reaction interphase as seen in **Figure 5.3**. At higher temperatures (1250°C) the depletion of Y into the molten glass is higher which explains the lower presence of garnets at the reaction layer and higher amount of dendritic garnets embedded in the glass, whereas the opposite process takes place at lower temperatures (1225°C). In addition to the depletion of garnet at 1250°C, the oxyapatite phase still remains stable acting as the main glass sealing product after long thermal exposure (>10 h.). In contrast, the effect of the temperature does not seem to make a significant impact in the infiltration depth of the glass as discussed in the following section.

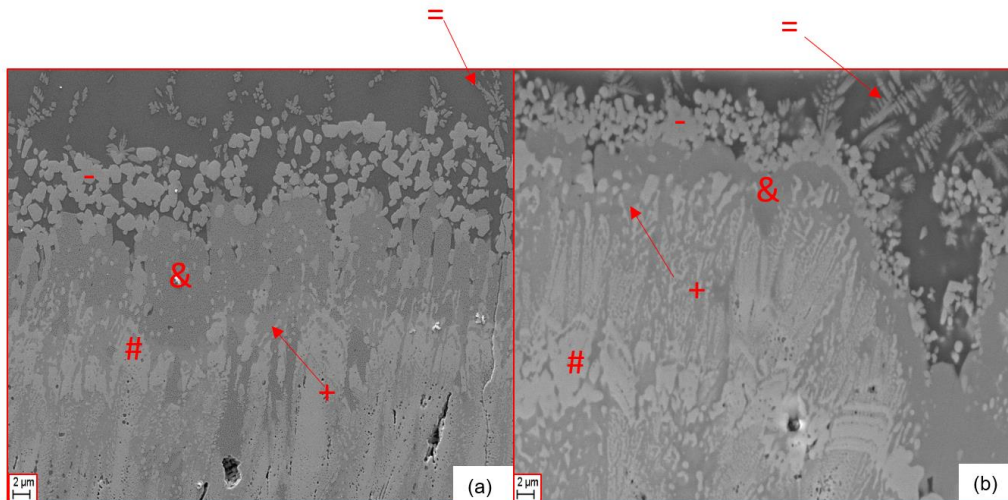


Figure 5.3: Reaction layer of Iceland VA at (a) 1225 and (b) 1250°C after 10 h. infiltration.

5.3.1 Infiltration Depth Analysis.

Figure 5.3.1 shows the max infiltration depth of the overall infiltrated area with respect to 1225 and 1250°C tests performed for 10 h. It is clear in the figure that the change in the infiltration depth is high for CMAS 1 with respect to change in temperature (almost double at 1250°C) among the other VA. This is mainly due to the melting nature and the high dependency of the crystalline constituents present in CMAS 1 which generate a narrow melting range of about 25°C. At 1225°C CMAS 1 is partially molten which restricts its ability to flow (very high viscosity). On the other hand, the volcanic ashes are already in completely molten state and exhibit higher viscosity which has a minimal change with respect to the 25°C temperature difference. That is the main reason why a difference in infiltration of about 6 - 8 μm for the performed thermal exposure tests was observed.

Figure 5.3.1 also shows very clearly the large influence of viscosity in the infiltration of the melt by showing how the lowest viscous fluid (CMAS 1) generates the deepest infiltration. At 1225°C CMAS 1 exhibits the lowest infiltration due to its partially molten state. In the case of

1250°C, CMAS 1 is fully molten and flows more freely into the coating influenced by its low viscosity.

In the case of Iceland VA, the difference in infiltration depth is the lowest (about 6 μm) which suggests that the combination of oxyapatite and garnet phases is effective against the temperature dependency. However, a depletion of garnets (&) at the TBC/molten glass interphase was found generated by a constant diffusion of Y into the deposited molten glass reservoir at 1250°C. The depletion of garnet phase promotes a more vigorous formation of oxyapatite in the interphase which keeps providing sealing properties. Also at deep glass infiltration areas the presence of oxyapatite products is higher suggesting its initial formation for crystallization. For Japan VA the main crystallization product present for the tested temperatures is oxyapatite which generates a minimal difference in infiltration. Finally, the difference in infiltration depth for VAs is governed by the viscosity of the molten glass. Iceland VA exhibits a lower viscosity, thus a higher infiltration than Japan VA.

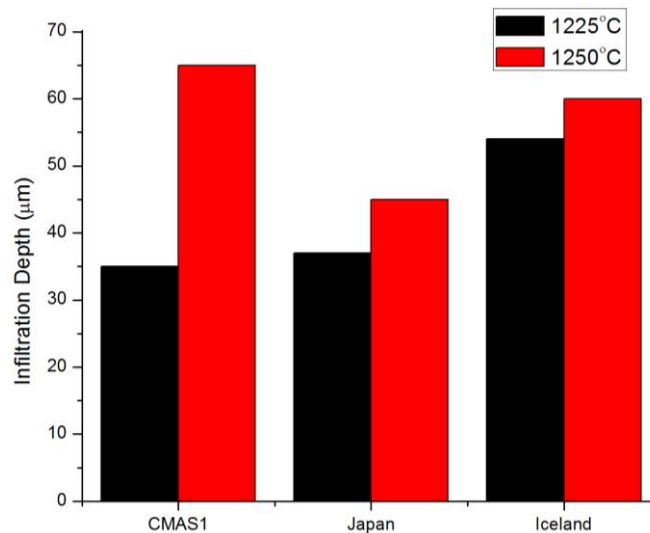


Figure 5.3.1: Infiltration depth for CMAS/VA for 10 h. infiltration tests.

5.3.2 Reaction Layer Growth.

Figure 5.3.2 shows the reaction layer growth for CMAS/VA after 10 h. infiltration at 1225 and 1250°C. The reaction layer growth exhibits a similar behavior to the infiltration depth showing the largest growth difference for CMAS 1 (17 μm) and lowest for Iceland VA (3 μm). In the case of CMAS 1 the large increase in reaction layer growth is governed by the availability of molten glass in order to generate formation of reaction products. For volcanic ashes, a slight difference is exhibited for the growth in reaction layer (6 to 3 μm). The minimal growth in reaction layer suggest that the oxyapatite product does not exhibit a temperature dependency and upon Y saturation it stabilizes avoiding extra Y diffusion.

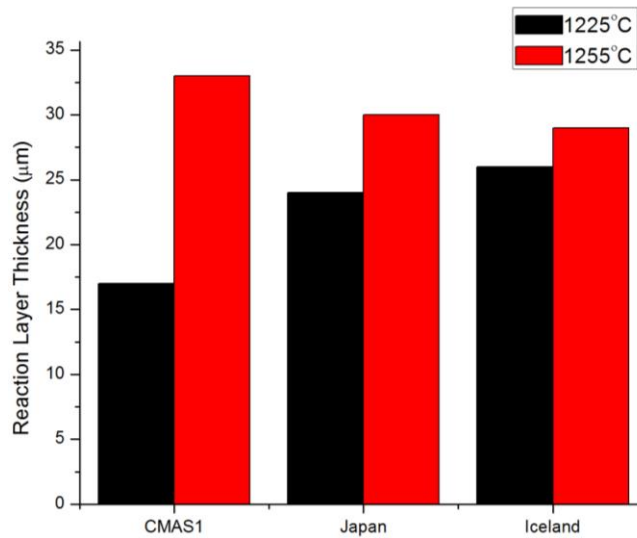


Figure 5.3.2: Reaction layer growth for CMAS/VA after 10 h. infiltration for 1225 and 1250°C.

Chapter 6: Conclusions

EB-PVD coatings based on a yttria-zirconia system (YSZ) with a nominal composition of 65 wt. % yttria were tested on lab scale under CMAS/VA infiltration for short term (5 min.) and long term infiltration (1-20 h.) in the temperature range from 1225 to 1250°C. Short term infiltration tests were performed on standard EB-PVD 7YSZ system and a physical model was proposed for infiltration kinetics. The infiltration results provided a comparison baseline for the mathematical infiltration model fitting. The mathematical model has considered all important parameters such as fluid properties (viscosity, surface tension, contact angle) and the TBC microstructure (permeability, tortuosity, pore fraction) which influence CMAS infiltration in TBCs.

The concentric pipe model with experimentally measured viscosity exhibited a good agreement with the experimental results for CMAS 1 infiltration therefore, confirming its higher realistic approach for EB-PVD systems compared with the standard open pipe model. The obtained results have showed a large discrepancy between the theoretical predicted viscosities (from the Giordano model) and the experimentally measured values. The model has confirmed the high influence of tortuosity in the infiltration by splitting the fluid path therefore, increasing significantly the time of infiltration. Concluding that an optimal CMAS resistant coating has to effectively combine a system where the viscosity of the melt is modified by inducing crystallization and the microstructure of the coating has to effectively split the path of the fluid therefore distributing it more efficiently to minimize the effects of infiltration.

The yttria rich coatings exhibited a higher CMAS resistance by inducing crystallization of CMAS/VA. It has formed stable reaction products sealing the gaps against infiltration and generated a uniform reaction layer at the TBC/molten glass interphase which exhibited a minimal growth with time. The previously reported beneficial effect of the oxyapatite and garnets formation on crystallization of molten glass in literature was confirmed in this work. The large presence of Fe in the glass promotes the formation a Fe-Y rich garnet which has not been

previously reported in literature. The overall infiltration of the glass was minimized by the vigorous reaction of the crystallization phases at the top interphase and columnar gaps. However, the microstructure of the coatings needs to be optimized for improved performance since at localized areas where large columnar gaps were available the glass infiltrated deeply into the coating. The diffusion of Y into the Fe rich glass for the case of the Iceland VA exhibits a higher activity in generating the garnet/dendritic particles at higher temperatures (1250°C) which generates a depletion in the garnet phase formed on the interphase after long term infiltration. Additionally, the high presence of Ca in CMAS 1 is believed to have major influence in the reaction layer growth by stabilizing the anorthite phase on top and generating a constant Fe-Y diffusion with respect to time.

Finally, the formation of Ca, Si, Mg, Al, Fe, Y, (Zr) bearing garnets with enrichments in Fe-Y are observed in this work where Fe is highly present in the glass. At low Fe availability (Japan VA), the formation of garnet is not found, making the oxyapatite phase with presence of Ca, Si, Y the main CMAS arrest phase. An assessment on the spallation behavior of the reaction layer has to be tested under thermal cycling tests and the optimal Y-Zr ratio for infiltration mitigation has to be determined.

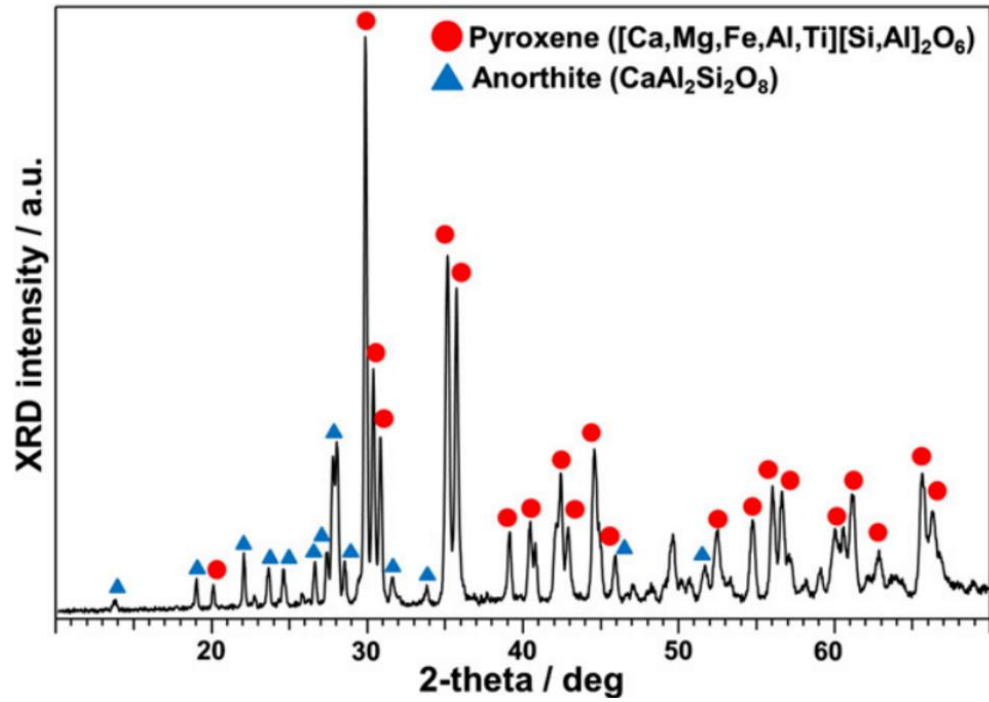
Works Cited

- [1] R. Dariola, "Thermal Barrier Coating Technology: Critical Review, Progress Update, Remaining Challenges and Prospects," *International Materials Reviews*, vol. 58, no. 6, pp. 315-348, 2013.
- [2] D. R. Clarke, M. Oechsner and N. P. Padture, "Thermal Barrier Coatings for More Efficient Gas-Turbine Engines," *MRS Bulletin*, vol. 37, no. 10, pp. 891-898, 2012.
- [3] N. P. Padture, M. Gell and E. H. Jordan, "Thermal Barrier Coatings for Gas-Turbine Engine Applications," *Science*, vol. 296, no. 5566, pp. 280-284, 2002.
- [4] Y. Tamarin, *Protective Coatings for Turbine Blades*, Materials Park, OH: ASM International, 2002.
- [5] T. M. Besmann, "Interface science for thermal barrier coatings," *Journal of Materials Science*, vol. 44, pp. 1661-1663, 2009.
- [6] X. Q. Cao, R. Vassen and R. Stoeber, "Ceramic materials for thermal barrier coatings," *Journal of the European Ceramic Society*, vol. 24, pp. 1-10, 2004.
- [7] E. Bakan, D. Emil, G. Mauer, R. Mucke and R. Vaben, "Porosity-Property Relationships of Plasma-Sprayed Gd₂Zr₂O₇/YSZ Thermal Barrier Coatings," *Journal of American Ceramic Society*, vol. 98, no. 8, pp. 2647-2654, 2015.
- [8] U. Schulz and W. Brave, "Degradation of La₂Zr₂O₇ and other novel EB-PVD thermal barrier coatings by CMAS (CaO-MgO-Al₂O₃-SiO₂) and volcanic ash deposits," *Surface & Coatings Technology*, vol. 235, pp. 165-173, 2013.
- [9] U. Schulz, B. Saruhan, K. Fritscher and C. Leyens, "Review on Advanced EB-PVD Ceramic Topcoats for TBC Applications," *International Journal of Applied Ceramic Technology*, vol. 1, no. 4, pp. 302-315, 2004.
- [10] J. R. Nicholls, K. J. Lawson, A. Johnstone and D. S. Rickerby, "Low Thermal Conductivity EB-PVD Thermal Barrier Coatings," *Materials Science Forum*, Vols. 369-372, pp. 595-606, 2001.
- [11] M. P. Borom, C. A. Johnson and L. A. Pleuso, "Role of Environmental Deposits and Operating Surface Temperature in Spallation of Air Plasma Sprayed Thermal Barrier Coatings," *Surface and Coatings Technology*, Vols. 86-87, pp. 116-126, 1996.
- [12] S. Krämer, J. Yang, C. G. Levi and C. A. Johnson, "Thermochemical Interaction of Thermal Barrier Coatings with Molten CaO-MgO-Al₂O₃-SiO₂ (CMAS) Deposits," *Journal of the American Ceramic Society*, vol. 89, no. 10, pp. 3167-3175, 2006.
- [13] G. Pujol, F. Ansart, J.-P. Bonino, A. Mailé and S. Hamadi, "Step-by-step investigation of degradation mechanisms induced by CMAS attack on YSZ materials for TBC applications," *Surface & Coatings Technology*, vol. 213, pp. 71-78, 2013.
- [14] K.-I. Lee, L. T. Wu, R. T. Wu and P. Xiao, "Mechanisms and mitigation of volcanic ash attack on yttria stabilized zirconia thermal barrier coatings," *Surface & Coatings Technology*, vol. 269, pp. 71-78, 2014.
- [15] A. K. Rai and R. S. Bhattacharya, "CMAS-Resistant Thermal Barrier Coatings (TBC)," *International Journal of Applied Ceramic Technology*, vol. 7, no. 5, pp. 662-674, 2010.
- [16] J. M. Drexler, A. L. Ortiz and N. P. Padture, "Composition effects of thermal barrier coating

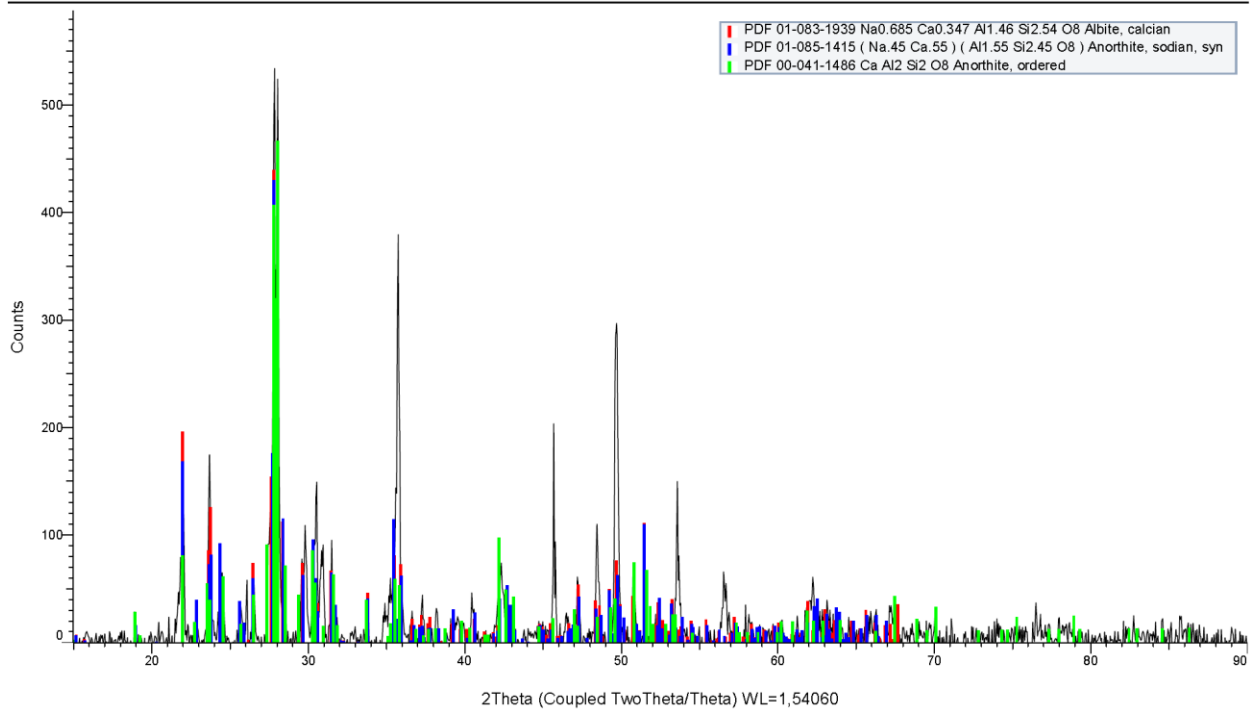
- ceramics on their interaction with molten Ca-Mg-Al-silicate (CMAS) glass," *Acta Materialia*, vol. 60, pp. 5437-5447, 2012.
- [17] R. C. Reed, *The Superalloys Fundamentals and Applications*, New York: Cambridge university press, 2006.
- [18] U. Kueppers, C. Cimorelli, K.-U. Hess, J. Taddeucci, F. B. Wadsworth and D. B. Dingwell, "The thermal stability of Eyjafjallajökull ash versus turbine ingestion test sands," *Journal of applied volcanology*, vol. 3, no. 4, pp. 1-11, 2014.
- [19] A. R. Krause, X. Li and N. P. Padture, "Interaction between ceramic powder and molten calcia-magnesia-alumino-silicate (CMAS) glass, and its implication on CMAS-resistant thermal barrier coatings," *Scripta Materialia*, vol. 112, pp. 118-122, 2016.
- [20] N. K. Elis, P. Mechnich and W. Braue, "Effect of CMAS Deposits on MOCVD Coatings in the System Y₂O₃-ZrO₂: Phase Relationships," *Journal of the american ceramic society*, pp. 1-8, 2013.
- [21] W. Li, H. Zhao, X. Zhong, L. Wang and S. Tao, "Air Plasma-Sprayed Ytria and Ytria-Stabilized Zirconia Thermal Barrier Coatings Subjected to Calcium-Magnesium-Alumino-Silicate (CMAS)," *Journal of Thermal Spray Technology*, vol. 23, no. 6, pp. 975-983, 2014.
- [22] C. Mercer, J. R. Williams, D. R. Clarke and A. G. Evans, "On a ferroelastic mechanism governing the toughness of the metastable tetragonal-prime (t') yttria-stabilized zirconia," *Proceedings of the royal society*, vol. 463, pp. 1393-1408, 2007.
- [23] A. C. Parlakyigit and A. C. Karaoglanli, "Effects of Microstructural Transformation in TBCs Consisting of NiCrAlY Metallic Bond Coat and YSZ Ceramic Top Coat after Oxidation at 900°C," *Acta Physica Polonica A*, vol. 125, 2014.
- [24] A. G. Evans, D. R. Munn, J. W. Hutchinson, G. H. Meier and F. S. Pettit, "Mechanisms controlling the durability of thermal barrier coatings," *Progress in Materials Science*, vol. 43, pp. 505-553, 2001.
- [25] P. K. Wright and A. G. Evans, "Mechanisms governing the performance of thermal barrier coatings," *Current Opinion in Solid State and Materials Science*, vol. 4, pp. 255-265, 1999.
- [26] J. A. Krogstad, Y. Gao, J. Bai, J. Wang, D. M. Lipkin and C. G. Levi, "In Situ Diffraction Study of the High-Temperature Decomposition of t'-Zirconia," *Journal of the american ceramic society*, vol. 98, no. 1, pp. 247-254, 2015.
- [27] U. Schulz, "Phase Transformation in EB-PVD Ytria Partially Stabilized Zirconia Thermal Barrier Coatings During Annealing," *Journal of the american ceramic society*, vol. 83, no. 4, pp. 904-910, 2000.
- [28] R. Subramanian, "Highly defective oxides as sinter resistant thermal barrier coatings". U.S. Patent 6,930,066, 2005.
- [29] L. Barbieri, F. Bondioli, I. Lancellotti, C. Leonelli, M. Montorsi, A. M. Ferrari and P. Mirselli, "The Anorthite-Diopside System: Structural and Devitrification Study. Part II: Crystallinity Analysis by the Rietveld RIR Method," *Journal of the American Ceramic Society*, vol. 88, no. 11, pp. 3131-3136, 2005.
- [30] W. Song, K.-U. Hess, D. E. Damby, F. B. Wadsworth, Y. Lavalley, C. Cimorelli and D. B. Dingwell, "Fusion characteristics of volcanic ash relevant to aviation hazards," *Geophysical Research Letters*, vol. 41, pp. 1-8, 2014.
- [31] E. M. Zaleski, C. Ensslen and C. G. Levi, "Melting and crystallization of silicate systems

- relevant to thermal barrier coating damage," *Journal of the american ceramic society*, vol. 98, no. 5, pp. 1642-1649, 2015.
- [32] L. Li and D. R. Clarke, "Effect of CMAS Infiltration on Radiative Transport Through an EB-PVD Thermal Barrier Coating," *International journal of applied ceramic technology*, vol. 5, no. 3, pp. 278-288, 2008.
- [33] C. Mercer, S. Faulhaber, A. G. Evans and R. Dariola, "A delamination mechanism for thermal barrier coatings subject to calcium-magnesium-alumino-silicate (CMAS) infiltration," *Acta Materialia*, vol. 53, pp. 1029-1039, 2005.
- [34] C. G. Levi, J. W. Hutchinson, M.-H. Vidal-Setif and C. A. Johnson, "Environmental degradation of thermal-barrier coatings by molten deposits," *MRS Bulletin*, vol. 37, pp. 932-941, 2012.
- [35] P. Mechnich, W. Braue and U. Schulz, "High-Temperature Corrosion of EB-PVD Yttria Partially Stabilized Zirconia Thermal Barrier Coatings with an Artificial Volcanic Ash Overlay," *Journal of the American Ceramic Society*, vol. 94, no. 3, pp. 925-931, 2011.
- [36] A. Aygun, A. L. Vasiliev, N. P. Padture and X. Ma, "Novel thermal barrier coatings that are resistant to high-temperature attack by glassy deposits," *Acta materialia*, vol. 55, pp. 6734-6745, 2007.
- [37] S. Krämer, J. Yang and C. G. Levi, "Infiltration-inhibiting reaction of gadolinium zirconate thermal barrier coatings with CMAS melts," *Journal of the american ceramic society*, vol. 91, no. 2, pp. 576-583, 2008.
- [38] A. R. Krause, H. F. Graces, B. S. Sentruk and N. P. Padture, "2ZrO₂.Y₂O₃ Thermal Barrier Coatings Resistant to Degradation by Molten CMAS: Part II, Interactions with Sand and Fly Ash," *Journal of the american ceramic society*, pp. 1-8, 2014.
- [39] V. L. Wiesner and N. P. Bansal, "Mechanical and thermal properties of calcium-magnesium-aluminosilicate (CMAS) glass," *Journal of the European Ceramic Society*, vol. 35, pp. 2907-2919, 2015.
- [40] Y. Yuan and T. R. Lee, "Contact Angle and Wetting Properties," in *Surface Science Techniques*, Springer, 2013, p. 663.
- [41] A. Kucuk, A. G. Clare and L. Jones, "An estimation of the surface tension for silicate glass melts at 1400C using statistical analysis," *Glass Technology*, vol. 40, no. 5, pp. 149-153, 1999.
- [42] D. Giordano, J. K. Russell and D. B. Dingwell, "Viscosity of magmatic fluids: A model," *Earth and Planetary Science Letters*, vol. 271, pp. 123-134, 2008.
- [43] W. Braue and P. Mechnich, "Recession of an EB-PVD coated turbine blade by CaSO₄ and Fe, Ti-rich CMAS-type deposits," *Journal of the american ceramic society*, vol. 94, no. 12, pp. 4483-4489, 2011.
- [44] R. Naraparaju, U. Schulz, P. Mechnich, P. Dobber and F. Seidel, "Degradation study of 7 wt.% yttria stabilised zirconia (7YSZ) thermal barrier coatings on aero-engine combustion chamber parts due to infiltration by different CaO-MgO-Al₂O₃-SiO₂ variants," *Surface & coatings technology*, vol. 260, pp. 73-81, 2014.
- [45] R. Naraparaju, P. Mechnich, U. Schulz and G. C. Mondragon Rodriguez, "The Accelerating Effect of CaSO₄ within CMAS (CaO-MgO-Al₂O₃-SiO₂) and its Effect on the Infiltration Behavior in EB-PVD 7YSZ," *Journal of the american ceramic society*, pp. 1-6, 2015.

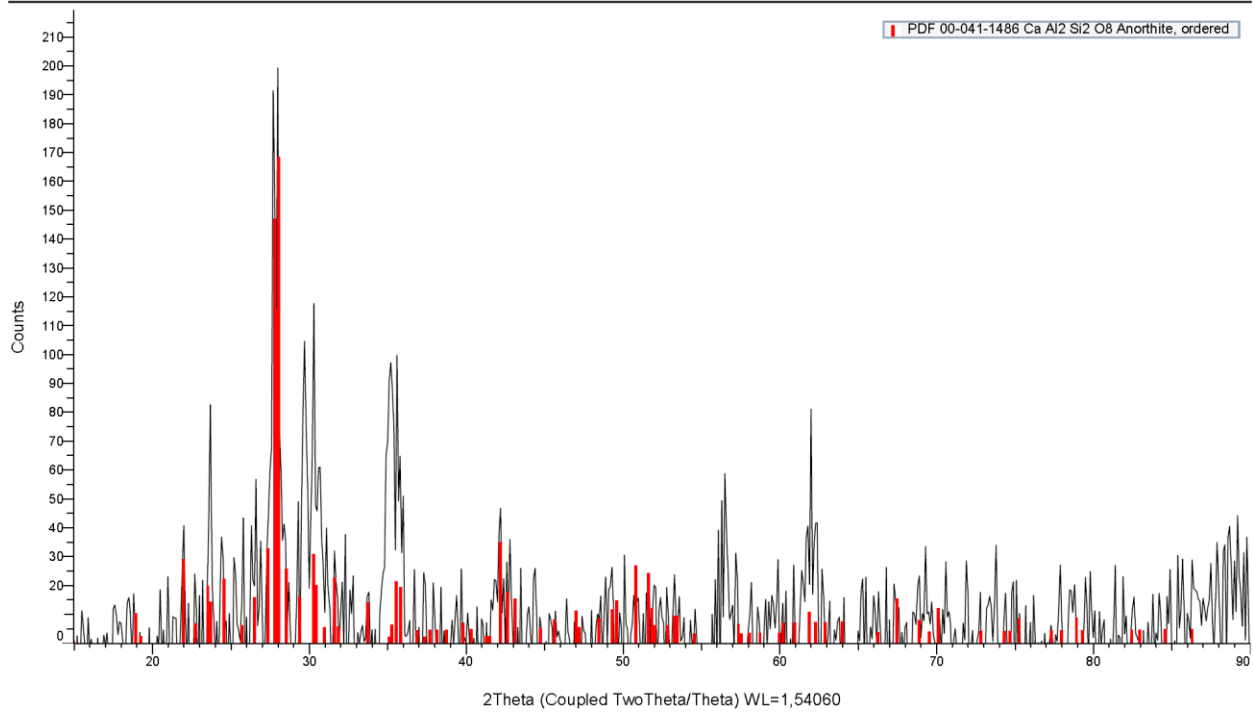
Appendix



Appendix 1: XDR pattern for CMAS 1 [44].



Appendix 2: XRD pattern for Japan VA.



Appendix 3: XRD pattern for Iceland VA.

Vita

Juan Jose Gomez was born in Delicias, Mexico. He received his bachelor of science (B.S.) in mechanical engineering from the University of Texas at El Paso (UTEP) on Summer 2014. During his undergraduate studies, he obtained several internships with power generation and steel industries in Mexico and the United States. After completion of his B.S. degree, he joined the Masters of Science program in Mechanical Engineering at UTEP where his research topics were focused on advanced materials for high temperature and energy conservation applications. As a graduate student, Juan Gomez was offered an internship position at the German Aerospace Center (DLR) in Cologne, Germany to work on his thesis project focused in high temperature novel materials for aerospace and energy applications. Upon graduation from Master's Degree on May 2016, he will be joining the Ph.D. program in Mechanical Engineering at UTEP to continue working on high temperature materials for aerospace and energy applications.

Permanent address: 1101 E. California Ave.
El Paso, Texas, 79902

This thesis/dissertation was typed by Juan Jose Gomez.